

# Local homeostatic regulation of the spectral radius of echo-state networks

Fabian Schubert<sup>1,\*</sup> and Claudius Gros<sup>1</sup>

<sup>1</sup>*Institute for Theoretical Physics, Goethe University Frankfurt am Main, Germany*

Correspondence\*:

Institute for Theoretical Physics  
Goethe University Frankfurt am Main  
Max-von-Laue-Str. 1  
60438 Frankfurt am Main, Germany  
fschubert@itp.uni-frankfurt.de

## ABSTRACT

Recurrent cortical networks provide reservoirs of states that are thought to play a crucial role for sequential information processing in the brain. However, classical reservoir computing requires manual adjustments of global network parameters, particularly of the spectral radius of the recurrent synaptic weight matrix. It is hence not clear if the spectral radius is accessible to biological neural networks.

Using random matrix theory, we show that the spectral radius is related to local properties of the neuronal dynamics whenever the overall dynamical state is only weakly correlated. This result allows us to introduce two local homeostatic synaptic scaling mechanisms, termed flow control and variance control, that implicitly drive the spectral radius towards the desired value. For both mechanisms the spectral radius is autonomously adapted while the network receives and processes inputs under working conditions.

We demonstrate the effectiveness of the two adaptation mechanisms under different external input protocols. Moreover, we evaluated the network performance after adaptation by training the network to perform a time-delayed XOR operation on binary sequences. As our main result, we found that flow control reliably regulates the spectral radius for different types of input statistics. Precise tuning is however negatively affected when interneural correlations are substantial. Furthermore, we found a consistent task performance over a wide range of input strengths/variances. Variance control did however not yield the desired spectral radii with the same precision, being less consistent across different input strengths.

Given the effectiveness and remarkably simple mathematical form of flow control, we conclude that self-consistent local control of the spectral radius via an implicit adaptation scheme is an interesting and biological plausible alternative to conventional methods using set point homeostatic feedback controls of neural firing.

**Keywords:** recurrent networks, homeostasis, synaptic scaling, echo-state networks, reservoir computing, spectral radius

## 1 INTRODUCTION

Cortical networks are highly recurrent, a property that is considered to be crucial for processing and storing temporal information. For recurrent networks to remain stable and functioning, the neuronal firing activity has to be kept within a certain range by autonomously active homeostatic mechanisms. It is hence important to study homeostatic mechanisms on the level of single neurons, as well as the more theoretic question of characterizing the dynamic state that is to be attained on a global network level. It is common to roughly divide adaptation mechanisms into intrinsic homeostasis, synaptic homeostasis, and metaplasticity.

Synaptic scaling was identified as a mechanism that can postsynaptically regulate neural firing by adjusting synaptic efficacies in a proportional, multiplicative way. This finding has led to numerous studies investigating the role of synaptic scaling in controlling neural network activity (Turrigiano et al., 1998; Turrigiano and Nelson, 2000; Turrigiano, 2008) and in stabilizing other plasticity mechanisms (van Rossum et al., 2000; Stellwagen and Malenka, 2006; Tetzlaff, 2011; Toyozumi et al., 2014). Indeed, synaptic scaling has proven successful in stabilizing activity in recurrent neural networks (Lazar et al., 2009; Remme and Wadman, 2012; Zenke et al., 2013; Effenberger and Jost, 2015; Miner and Triesch, 2016). However, these studies either used synaptic scaling as the sole homeostatic mechanism (Zenke et al., 2013; Remme and Wadman, 2012) or resorted to a variant of synaptic scaling where the scaling is not dynamically determined through a control loop using a particular target activity, but rather by a fixed multiplicative normalization rule (Lazar et al., 2009; Effenberger and Jost, 2015; Miner and Triesch, 2016). Therefore, these homeostatic models cannot account for higher moments of temporal activity patterns, i.e., their variance, as this would require at least the tuning of two parameters (Cannon and Miller, 2017).

Within more abstract models of rate encoding neurons, intrinsic homeostasis and synaptic scaling essentially correspond to adjusting a bias and gain factor on the input entering a nonlinear transfer function. Within this framework, multiple dual-homeostatic adaptation rules have been investigated concerning their effect on network performance. In this framework, the adaptation of the bias acts as an intrinsic plasticity mechanism for the control of the internal excitability of a neuron (Franklin et al., 1992; Abbott and LeMasson, 1993; Borde et al., 1995), while the gain factors functionally correspond to a synaptic scaling of the recurrent weights. Learning rules for these types of models were usually derived by defining a target output distribution that each neuron attempts to reproduce by changing neural gains and biases (Triesch, 2007; Steil, 2007; Schrauwen et al., 2008; Boedecker et al., 2009), or were directly derived from an information-theoretic measure (Bell and Sejnowski, 1995).

While these studies did indeed show performance improvements by optimizing local information transmission measures, apparently, optimal performance can effectively be traced back to a global parameter, the spectral radius of the recurrent weight matrix (Schrauwen et al., 2008). Interestingly, to our knowledge, theoretical studies on spiking neural networks did not explicitly consider the spectral radius as a parameter affecting network dynamics. Still, the theory of balanced states in spiking recurrent networks established the idea that synaptic strengths should scale with  $1/\sqrt{k}$ , where  $k$  is the average number of afferent connections (Van Vreeswijk and Sompolinsky, 1998). According to the circular law of random matrix theory, this scaling rule simply implies that the spectral radius of the recurrent weight matrix remains finite as the number of neurons  $N$  increases. More recent experiments on cortical cultures confirm this scaling (Barral and D'Reyes, 2016).

In the present study, we investigated whether the spectral radius of the weight matrix in a random recurrent network can be regulated by a combination of intrinsic homeostasis and synaptic scaling. Following the standard echo-state framework, we used rate encoding tanh-neurons as the model of choice. However, aside from their applications as efficient machine learning algorithms, echo state networks are potentially

relevant as models of information processing in the brain (Nikolić et al., 2009; Hinaut et al., 2015; Enel et al., 2016). Note in this context that extensions to layered ESN architectures have been presented by Gallicchio and Micheli (2017), which bears a somewhat greater resemblance to the hierarchical structure of cortical networks than the usual shallow ESN architecture. This line of research illustrates the importance of examining whether local and biological plausible principles exist that would allow to tune the properties of the neural reservoir to the “edge of chaos” (Livi et al., 2018), particularly when a continuous stream of inputs is present. The rule has to be independent of both the network topology, which is not locally accessible information, and the distribution of synaptic weights.

We propose and compare two unsupervised homeostatic mechanisms, which we denote by flow control and variance control. Both regulate the mean and variance of neuronal firing such that the network works in an optimal regime concerning sequence learning tasks. The mechanisms act on two sets of node-specific parameters, the biases  $b_i$ , and the neural gain factors  $a_i$ . We restricted ourselves to biologically plausible adaptation mechanisms, viz adaptation rules for which the dynamics of all variables are local, i.e., bound to a specific neuron. Additional variables enter only when locally accessible. In a strict sense, this implies that local dynamics are determined exclusively by the neuron’s dynamical variables and by information about the activity of afferent neurons. Being less restrictive, one could claim that it should also be possible to access aggregate or mean-field quantities that average a variable of interest over the population. For example, nitric oxide is a diffusive neurotransmitter that can act as a measure for the population average of neural firing rates (Sweeney et al., 2015).

Following a general description of the network model, we introduce both adaptation rules and evaluate their effectiveness in tuning the spectral radius in Section 2.4 and 2.5. We assess the performance of networks that were subject to adaptation in Section 2.7, using a nonlinear sequential memory task. Finally, we discuss the influence of node-to-node cross-correlations within the population in Section 2.8.

## 2 RESULTS

### 2.1 Model

A full description of the network model and parameters can be found in the methods section. We briefly introduce the network dynamics as

$$x_i(t) = x_{r,i}(t) + I_i(t) \quad (1)$$

$$x_{r,i}(t) := a_i \sum_{j=1}^N W_{ij} y_j(t-1) \quad (2)$$

$$y_i(t) = \tanh(x_i(t) - b_i) . \quad (3)$$

Each neuron’s membrane potential  $x_i$  consists of a recurrent contribution  $x_{r,i}(t)$  and an external input  $I_i(t)$ . The biases  $b_i$  are subject to the following homeostatic adaptation:

$$b_i(t) = b_i(t-1) + \epsilon_b [y_i(t) - \mu_t] . \quad (4)$$

Here,  $\mu_t$  defines a target for the average activity and  $\epsilon_b$  is the adaptation rate.

The local parameters  $a_i$  act as scaling factors on the recurrent weights. We considered two different forms of update rules. Loosely speaking, both drive the network towards a certain dynamical state which corresponds to the desired spectral radius. The difference between them lies in the variables characterizing

this state: While flow control defines a relation between the variance of neural activity and the variance of the total recurrent synaptic current, variance control does so by a more complex relation between the variance of neural activity and the variance of the synaptic current from the external input.

### 2.1.1 Flow control

The first adaptation rule, flow control, is given by

$$a_i(t) = a_i(t-1) \left[ 1 + \epsilon_a \Delta R_i(t) \right], \quad \Delta R_i(t) = R_t^2 y_i^2(t-1) - x_{r,i}^2(t). \quad (5)$$

The parameter  $R_t$  is the desired target spectral radius and  $\epsilon_a$  the adaptation rate of the scaling factor. The dynamical variables  $y_i^2$  and  $x_{r,i}^2$  have been defined before in Eqs. (1) and (2). We also considered an alternative global update rule where  $\Delta R_i(t)$  is given by

$$\Delta R_i(t) = \frac{1}{N} \left[ R_t^2 \|\mathbf{y}(t-1)\|^2 - \|\mathbf{x}_r(t)\|^2 \right], \quad (6)$$

where  $\|\cdot\|$  denotes the euclidean vector norm. However, since this is a non-local rule, it only served as a comparative model to Eq. (5) when we investigated the effectiveness of the adaptation mechanism. Three key assumptions enter flow control, Eq. (5):

- Represented by  $x_{r,i}(t)$ , we assume that there is a physical separation between the recurrent input that a neuron receives and its external inputs. This is necessary because  $x_{r,i}(t)$  is explicitly used in the update rule of the synaptic scaling factors.
- Synaptic scaling only affects the weights of recurrent connections. However, this assumption is not crucial for the effectiveness of our plasticity rule, as we were mostly concerned with achieving a preset spectral radius for the recurrent weight matrix. If instead the scaling factors acted on both the recurrent and external inputs, this would lead to an “effective” external input  $I'_i(t) := a_i I_i(t)$ . However,  $a_i$  only affecting the recurrent input facilitated the parameterization of the external input by means of its variance, see Section 2.7, a choice of convenience.
- For (5) to function, neurons need to be able to represent and store squared neural activities.

Whether these three preconditions are satisfied by biological neurons needs to be addressed in future studies.

### 2.1.2 Variance control

The second adaptation rule, variance control, has the form

$$a_i(t) = a_i(t-1) + \epsilon_a \left[ \sigma_{t,i}^2(t) - (y_i(t) - \mu_i^y(t))^2 \right] \quad (7)$$

$$\sigma_{t,i}^2(t) = 1 - \frac{1}{\sqrt{1 + 2R_t^2 y_i(t)^2 + 2\sigma_{\text{ext},i}^2(t)}}. \quad (8)$$

Eq. (7) drives the average variance of each neuron towards a desired target variance  $\sigma_{t,i}^2(t)$  at an adaptation rate  $\epsilon_a$  by calculating the momentary squared difference between the local activity  $y_i(t)$  and its trailing average  $\mu_i^y(t)$ . Eq. (8) calculates the target variance as a function of the target spectral radius  $R_t$ , the current local square activity  $y_i^2(t)$  and a trailing average  $\sigma_{\text{ext},i}^2(t)$  of the local variance of the external input signal. When all  $a_i(t)$  reach a steady state, the average neural variance equals the target given by (8). According to

a mean-field approach that is described in Section 5.6, reaching this state then results in a spectral radius  $R_a$  that is equal to the target  $R_t$  entering (8). Intuitively, it is to be expected that  $\sigma_{t,i}^2$  is a function of both the spectral radius and the external driving variance: The amount of fluctuations in the network activity is determined by the dynamic interplay between the strength of the external input as well as the recurrent coupling.

A full description of the auxiliary equations and variables used to calculate  $\mu_i^y(t)$  and  $\sigma_{\text{ext},i}^2(t)$  can be found in Section 5.1.

Similar to flow control, we also considered a non-local version for comparative reasons, where (8) is replaced with

$$\sigma_{t,i}^2(t) = 1 - \frac{1}{\sqrt{1 + 2R_t^2 \|\mathbf{y}(t)\|^2/N + 2\sigma_{\text{ext},i}^2(t)}}. \tag{9}$$

Again,  $\|\cdot\|$  denotes the euclidean norm. Before proceeding to the results, we discuss the mathematical background of the proposed adaptation rules in some detail.

## 2.2 Autonomous spectral radius regulation

There are some interesting aspects to the theoretical framework at the basis of the here proposed regulatory scaling mechanisms.

The circular law of random matrix theory states that the eigenvalues  $\lambda_j$  are distributed uniformly on the complex unit disc if the elements of a real  $N \times N$  matrix are drawn from distributions having zero mean and standard deviation  $1/\sqrt{N}$  (Tao and Vu, 2008). Given that the internal weight matrix  $\widehat{W}$  ( $\widehat{\cdot}$  denoting matrices) with entries  $W_{ij}$  has  $p_r N$  non-zero elements per row ( $p_r$  is the connection probability), the circular law implies that the spectral radius of  $a_i W_{ij}$ , the maximum of  $|\lambda_j|$ , is unity when the synaptic scaling factors  $a_i$  are set uniformly to  $1/\sigma_w$ , where  $\sigma_w$  is the standard deviation of  $W_{ij}$ . Our goal is to investigate adaptation rules for the synaptic scaling factors that are based on dynamic quantities, which includes the membrane potential  $x_i$ , the neural activity  $y_i$  and the input  $I_i$ .

The circular law, i. e. a  $N \times N$  matrix with i.i.d. entries with zero mean and  $1/N$  variance approaching a spectral radius of one as  $N \rightarrow \infty$ , can be generalized. Rajan and Abbott (2006) investigated the case where the statistics of the columns of the matrix differ in their means and variances: given row-wise E-I balance for the recurrent weights, the square of the spectral radius of a random  $N \times N$  matrix whose columns have variances  $\sigma_i^2$  is  $N \langle \sigma_i^2 \rangle_i$  for  $N \rightarrow \infty$ . Since the eigenvalues are invariant under transposition, this result also holds for row-wise variations of variances and column-wise E-I balance. While the latter is not explicitly enforced in our case, deviations from this balance are expected to tend to zero for large  $N$  given the statistical assumptions that we made about the matrix elements  $W_{ij}$ . Therefore, the result can be applied to our model, where node-specific gain factors  $a_i$  are applied to each row of the recurrent weight matrix. Thus, the spectral radius  $R_a$  of the *effective random matrix*  $\widehat{W}_a$  with entries  $a_i W_{ij}$  (as entering (2)) is

$$R_a^2 \approx \frac{1}{N} \sum_i R_{a,i}^2, \quad R_{a,i}^2 := a_i^2 \sum_j (W_{ij})^2, \tag{10}$$

for large  $N$ , when assuming that the distribution underlying the *bare weight matrix*  $\widehat{W}$  with entries  $W_{ij}$  has zero mean. Note that  $R_a^2$  can be expressed alternatively in terms of the Frobenius norm  $\|\widehat{W}_a\|_F$ , via

$$R_a^2 \approx \|\widehat{W}_a\|_F^2 / N. \tag{11}$$

We numerically tested Eq. (10) for  $N = 500$  and heterogeneous random sets of  $a_i$  drawn from a uniform  $[0, 1]$ -distribution and found a very close match to the actual spectral radii (1-2% relative error). Given that the  $R_{a,i}$  can be interpreted as per-site estimates for the spectral radius, one can use the generalized circular law (10) to regulate  $R_a$  on the basis of local adaptation rules, one for every  $a_i$ .

For the case of flow control, the adaptation rule is derived using a comparison between the variance of neural activity that is present in the network with the recurrent contribution to the membrane potential. A detailed explanation is presented in Section 2.6 and Section 5.5. In short, we propose that

$$\langle \|\mathbf{x}_r(t)\|^2 \rangle_t \cong R_a^2 \langle \|\mathbf{y}(t-1)\|^2 \rangle_t, \quad (12)$$

where  $x_{r,i}$  is the recurrent contribution to the membrane potential  $x_i$ . This stationarity condition leads to the adaptation rule given in Eq. (5). An analysis of the dynamics of this adaptation mechanisms can be found in Section 5.5.

Instead of directly imposing Eq. (12) via an appropriate adaptation mechanism, we also considered the possibility of transferring this condition into a set point for the variance of neural activities as a function the external driving. To do so, we used a mean-field approach to describe the effect of recurrent input onto the resulting neural activity variance. An in-depth discussion is given in Section 5.6. This led to the update rule given by Eq. (7) and (8) for variance control.

### 2.3 Testing protocols

We used several types of input protocols for testing the here proposed adaptation mechanisms, as well as for assessing the task performance discussed in Section 2.7. The first two variants concern distinct biological scenarios:

- *Binary*. Binary input sequences correspond to a situation when a neural ensemble receives input dominantly from a singular source, which itself has only two states, being either active or inactive. Using binary input sequences during learning is furthermore consistent with the non-linear performance test considered here for the echo-state network as a whole, the delayed XOR-task. See Section 2.7. For symmetric binary inputs, as used, the source signal  $u(t)$  is drawn from  $\pm 1$ .
- *Gaussian*. Alternatively one can consider the situation that a large number of essentially uncorrelated input streams are integrated. This implies random Gaussian inputs signals. Neurons receive in this case zero-mean independent Gaussian noise.

Another categorical dimension concerns the distribution of the afferent synaptic weights. Do all neurons receive inputs with the same strength, or not? As a quantifier for the individual external input strengths, the variances  $\sigma_{\text{ext},i}^2$  of the local external input currents were taken into account. We distinguished two cases

- *Heterogeneous*. In the first case, the  $\sigma_{\text{ext},i}^2$  are quenched random variables. This means that each neuron is assigned a random value  $\sigma_{\text{ext},i}^2$  before the start of the simulation, as drawn from a half-normal distribution parameterized by  $\sigma = \sigma_{\text{ext}}$ . This ensures that the expected average variance  $\langle \sigma_{\text{ext},i}^2 \rangle$  is given by  $\sigma_{\text{ext}}^2$ .
- *Homogeneous*. In the second case, all  $\sigma_{\text{ext},i}^2$  are assigned the identical global value  $\sigma_{\text{ext}}^2$ .

Overall, pairing “binary” vs. “Gaussian” and “heterogeneous” vs. “homogeneous”, leads to a total of four different input protocols, i. e. “heterogeneous binary”, “homogeneous binary”, “heterogeneous

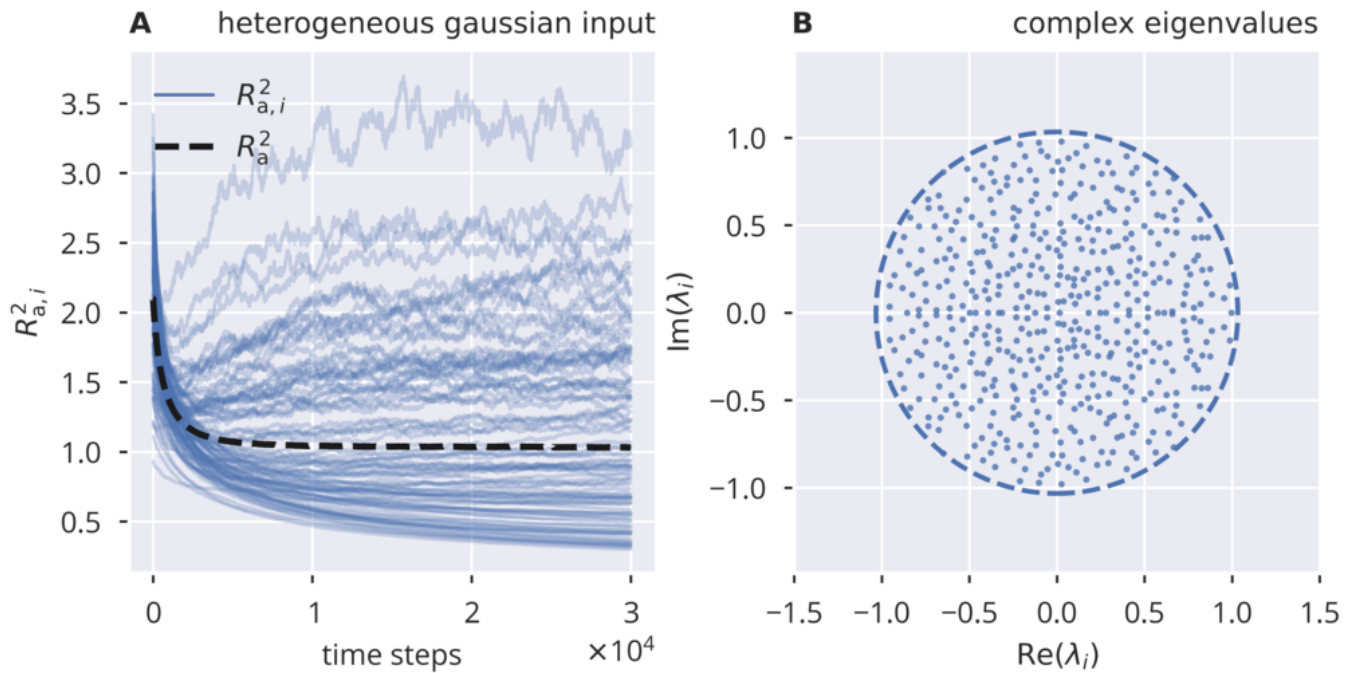


**Figure 1. Online spectral radius regulation using flow control.** The spectral radius  $R_a$  and the respective local estimates  $R_{a,i}$  as defined by (10). For the input protocol see Section 5.3. **A:** Dynamics of  $R_{a,i}^2$  and  $R_a^2$ , in the presence of heterogeneous independent Gaussian inputs. Local adaptation. **B:** Distribution of eigenvalues of the corresponding effective synaptic matrix  $\widehat{W}_a$ , after adaptation. The circle denotes the spectral radius.

Gaussian” and “homogeneous Gaussian”. If not otherwise stated, numerical simulations were done using networks with  $N = 500$  sites and a connection probability  $p_r = 0.1$ .

### 2.4 Performance testing of flow control

In Figure 1, we present a simulation using flow control for heterogeneous Gaussian input with an adaptation rate  $\epsilon_a = 10^{-3}$ . The standard deviation of the external driving was set to  $\sigma_{\text{ext}} = 0.5$ . The spectral radius of  $R_a$  of  $\widehat{W}_a$  was tuned to the target  $R_t = 1$  with high precision, even though the local, row-wise estimates  $R_{a,i}$  showed substantial deviations from the target.

We further tested the adaptation with other input protocols, see Section 2.3 and Figure 11. We found that flow control robustly led to the desired spectral radius  $R_t$  under all Gaussian input protocols, while binary input caused  $R_a$  to converge to higher values than  $R_t$ . However, when using global adaptation, as given by Eq. (6), all input protocols resulted in the correctly tuned spectral radius, see Figure 12.

Numerically, we found that the time needed to converge to the stationary states depended substantially on  $R_t$ , slowing down when the spectral radius becomes small. It is then advantageous, as we have done, to scale the adaptation rate  $\epsilon_a$  inversely with the trailing average  $\bar{x}_r^2$  of  $\|x_r\|^2$ , viz as  $\epsilon_a \rightarrow \epsilon_a / \bar{x}_r^2$ . An exemplary plot showing the effect of this scaling is shown in Fig. 7, see Section 5.2 for further details.

To evaluate the amount of deviation from the target spectral radius under different input strengths and protocols, we plotted the difference between the resulting spectral radius and the target spectral radius for a range of external input strength, quantified by their standard deviation  $\sigma_{\text{ext}}$ . Results for different input protocols are shown in Figure 15 in the supplementary material. For correlated binary input, increasing the

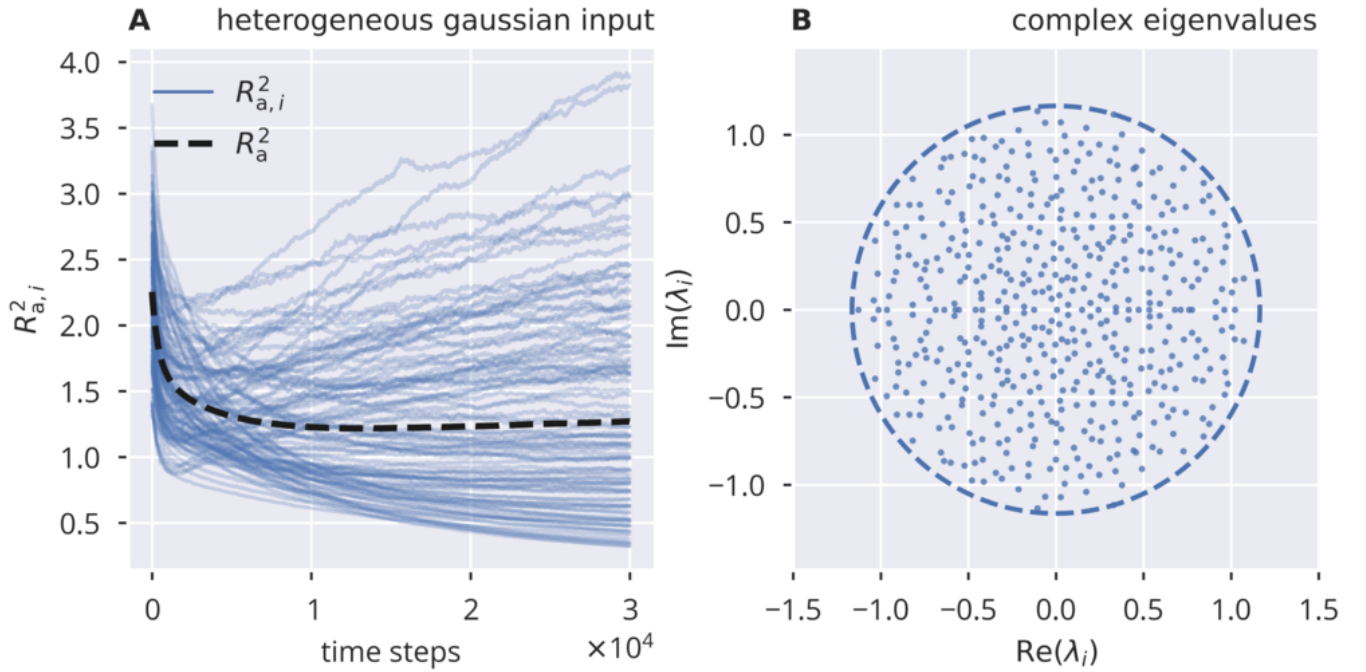


**Figure 2. Online spectral radius regulation using variance control.** The spectral radius  $R_a$  and the respective local estimates  $R_{a,i}$  as defined by (10). For the input protocol see Section 5.3. **A:** Dynamics of  $R_{a,i}^2$  and  $R_a^2$ , in the presence of heterogeneous independent Gaussian inputs. Local adaptation. **B:** Distribution of eigenvalues of the corresponding effective synaptic matrix  $\widehat{W}_a$ . The circles denote the respective spectral radius.

input strength resulted in stronger deviations from the target spectral radius. On the other hand, uncorrelated Gaussian inputs resulted in perfect alignment for the entire range of input strengths that we tested.

## 2.5 Performance testing of variance control

In comparison, variance control, shown in Figure 2 and Figure 13, resulted in notable deviations from  $R_t$ , for both uncorrelated Gaussian and correlated binary input. As for flow control, we also calculated the deviations from  $R_t$  as a function of  $\sigma_{\text{ext}}$ , see Figure 16. For heterogeneous binary input, deviations from the target spectral radius did not increase monotonically as a function of the input strength (Figure 16A), reaching a peak at  $\sigma_{\text{ext}} \approx 0.4$  for target spectral radii larger than 1. For homogeneous binary input, we observed a substantial negative mismatch of the spectral radius for strong external inputs, see Figure 16C.

Overall, we found that variance control did not exhibit the same level of consistency in tuning the system towards a desired spectral radius, even though it did perform better in some particular cases (compare Figure 15A for large  $\sigma_{\text{ext}}$  with Figure 16). Moreover, variance control exhibited deviations from the target (shown in Figure 14) even when a global adaptation rule was used, as defined in (9). This is in contrast to the global variant of flow control, which, as stated in the previous section, robustly tuned the spectral radius to the desired value even in the presence of strongly correlated inputs.

## 2.6 Spectral radius, singular values and global Lyapunov exponents

Apart from the spectral radius  $R_a$  of the matrix  $\widehat{W}_a$ , one may consider the relation between the adaptation dynamics and the respective singular values  $\sigma_i$  of  $\widehat{W}_a$ . We recall that the spectrum of  $\hat{U}_a = \widehat{W}_a^\dagger \widehat{W}_a$  is given by the squared singular values,  $\sigma_i^2$ , and that the relation  $\|\mathbf{x}_r\|^2 = \mathbf{y}^\dagger \widehat{W}_a^\dagger \widehat{W}_a \mathbf{y}$  holds. Now, assume that the



time-averaged projection of neural activity  $\mathbf{y} = \mathbf{y}(t)$  onto all eigenvectors of  $\hat{U}_a$  is approximately the same, that is, there is no preferred direction of neural activity in phase space. From this idealized case, it follows that the time average of the recurrent contribution to the membrane potential can be expressed with

$$\langle \|\mathbf{x}_r\|^2 \rangle_t \approx \frac{\langle \|\mathbf{y}\|^2 \rangle_t}{N} \sum_i \sigma_i^2 = \frac{\langle \|\mathbf{y}\|^2 \rangle_t}{N} \sum_{i,j} (a_i W_{ij})^2 \tag{13}$$

as the rescaled average of the  $\sigma_i^2$ . For the second equation, we used the fact that the  $\sum_i \sigma_i^2$  equals the sum of all matrix elements squared (Sengupta and Mitra, 1999; Shen, 2001). With (10), one finds that (13) is equivalent to  $\langle \|\mathbf{x}_r\|^2 \rangle_t = R_a^2 \langle \|\mathbf{y}\|^2 \rangle_t$  and hence to the flow condition (12). This result can be generalized, as done in Section 5.5, to the case that the neural activities have inhomogeneous variances, while still being uncorrelated with zero mean. We have thus shown that the stationarity condition leads to a spectral radius of (approximately) unity.

It is worthwhile to note that the singular values of  $\hat{U}_a = \widehat{W}_a^\dagger \widehat{W}_a$  do exceed unity when  $R_a = 1$ . More precisely, for a random matrix with i.i.d. entries, one finds in the limit of large  $N$  that the largest singular value is given by  $\sigma_{\max} = 2R_a$ , in accordance with the Marchenko-Pastur law for random matrices (Marčenko and Pastur, 1967). Consequently, directions in phase space exist in which the norm of the phase space vector is elongated by factors greater than one. Still, this does not contradict the fact that a unit spectral radius coincides with the transition to chaos for the non-driven case. The reason is that the global Lyapunov exponents are given by

$$\lim_{n \rightarrow \infty} \frac{1}{2n} \ln \left( \left( \widehat{W}_a^n \right)^\dagger \widehat{W}_a^n \right) \tag{14}$$

which eventually converge to  $\ln \|\lambda_i\|$ , see Figure 17 in the supplementary material and Wernecke et al. (2019), where  $\lambda_i$  is the  $i$ th eigenvalue of  $\widehat{W}_a$ . The largest singular value of the  $n$ th power of a random matrix with a spectral radius  $R_a$  scales like  $R_a^n$  in the limit of large powers  $n$ . The global Lyapunov exponent goes to zero as a consequence when  $R_a \rightarrow 1$ .

## 2.7 XOR-memory recall

To this point, we presented results regarding the effectiveness of the introduced adaptation rules. However, we did not account for their effects onto a given learning task. Therefore, we tested the performance of locally adapted networks under the delayed XOR task, which evaluates the memory capacity of the echo state network in combination with a non-linear operation. For the task, the XOR operation is to be taken with respect to a delayed pair of two consecutive binary inputs signals,  $u(t-\tau)$  and  $u(t-\tau-1)$ , where  $\tau$  is a fixed time delay. The readout layer is given by a single unit, which has the task of reproducing

$$f_\tau(t) = \text{XOR} [u(t-\tau), u(t-\tau-1)], \quad t, \tau = 1, 2, \dots, \tag{15}$$

where  $\text{XOR}[u, u']$  is 0/1 if  $u$  and  $u'$  are identical/not identical.

The readout vector  $\mathbf{w}_{\text{out}}$  is trained with respect to the mean squared output error,

$$\|\widehat{Y} \mathbf{w}_{\text{out}} - \mathbf{f}_\tau\|^2 + \alpha \|\mathbf{w}_{\text{out}}\|^2, \tag{16}$$

using ridge regression on a sample batch of  $T_{\text{batch}} = 10N$  time steps, here for  $N = 500$ , and a regularization factor of  $\alpha = 0.01$ . The batch matrix  $\widehat{Y}$ , of size  $T_{\text{batch}} \times (N + 1)$ , holds the neural activities as well as one node with constant activity serving as a potential bias. Similarly, the readout (column) vector  $\mathbf{w}_{\text{out}}$  is of

size  $(N + 1)$ . The  $T_{\text{batch}}$  entries of  $\mathbf{f}_\tau$  are the  $f_\tau(t)$ , viz the target values of the XOR problem. Minimizing (16) leads to

$$\mathbf{w}_{\text{out}} = \left( \hat{Y}^\dagger \hat{Y} + \alpha^2 \hat{\mathbf{1}} \right)^{-1} \hat{Y}^\dagger \mathbf{f}_\tau. \quad (17)$$

The learning procedure was repeated independently for each time delay  $\tau$ . We quantified the performance by the total memory capacity,  $\text{MC}_{\text{XOR}}$ , as

$$\text{MC}_{\text{XOR}} = \sum_{k=1}^{\infty} \text{MC}_{\text{XOR},k} \quad (18)$$

$$\text{MC}_{\text{XOR},k} = \frac{\text{Cov}^2 [f_k(t), y_{\text{out}}(t)]_t}{\text{Var} [f_k(t)]_t \text{Var} [y_{\text{out}}(t)]_t}. \quad (19)$$

This is a simple extension of the usual definition of short term memory in the echo state literature (Jaeger, 2002). The activity  $y_{\text{out}} = \sum_{i=1}^{N+1} w_{\text{out},i} y_i$  of the readout unit is compared in (19) with the XOR prediction task, with the additional neuron,  $y_{N+1} = 1$ , corresponding to the bias of the readout unit. Depending on the mean level of the target signal, this offset might actually be unnecessary. However, since it is a standard practice to use an intercept variable in linear regression models, we decided to include it into the readout variable  $y_{\text{out}}$ . The variance and covariance are calculated with respect to the batch size  $T_{\text{batch}}$ .

The results for flow control presented in Figure 3 correspond to two input protocols, heterogeneous Gaussian and binary inputs. Shown are sweeps over a range of  $\sigma_{\text{ext}}$  and  $R_t$ . The update rule (5) was applied to the network for each pair of parameters until the  $a_i$  values converged to a stable configuration. We then measured the task performance as described above. Note that in the case of Gaussian input, this protocol was only used during the adaptation phases. Due to the nature of the XOR task, binary inputs with the corresponding variances are to be used during performance testing. See Figure 18 in the supplementary material for a performance sweep using the homogeneous binary and Gaussian input protocol. Optimal performance was generally attained around the  $R_a \approx 1$  line. A spectral radius  $R_a$  slightly smaller than unity was optimal when using Gaussian input, but not for binary input signals. In this case the measured spectral radius  $R_a$  deviated linearly from the target  $R_t$ , with increasing strength of the input, as parameterized by the standard deviation  $\sigma_{\text{ext}}$ . Still, the locus of optimal performance was essentially independent of the input strength, with maximal performance attained roughly at  $R_t \approx 0.55$ . Note that the line  $R_a = 1$  joins  $R_t = 1$  in the limit  $\sigma_{\text{ext}} \rightarrow 0$ .

Comparing these results to variance control, as shown in Figure 4, we found that variance control led to an overall lower performance. To our surprise, for external input with a large variance, Gaussian input caused stronger deviations from the desired spectral radius as compared to binary input. Therefore, in a sense, it appeared to behave opposite to what we found for flow control. However, similar to flow control, the value of  $R_t$  giving optimal performance under a given  $\sigma_{\text{ext}}$  remained relatively stable over the range of external input strength measured. On the other hand, using homogeneous input, see Figure 19 in the supplementary material, did cause substantial deviations from the target spectral radius when using binary input.

## 2.8 Input induced correlations

A crucial assumption leading to the proposed adaptation rules is the statistical independence of neural activity for describing the statistical properties of the bare recurrent contribution to the membrane potential,  $x_{\text{bare}} = \sum_j W_{ij} y_j$ . In particular, the variance  $\sigma_{\text{bare}}^2$  of  $x_{\text{bare}}$  enters the mean-field approach described

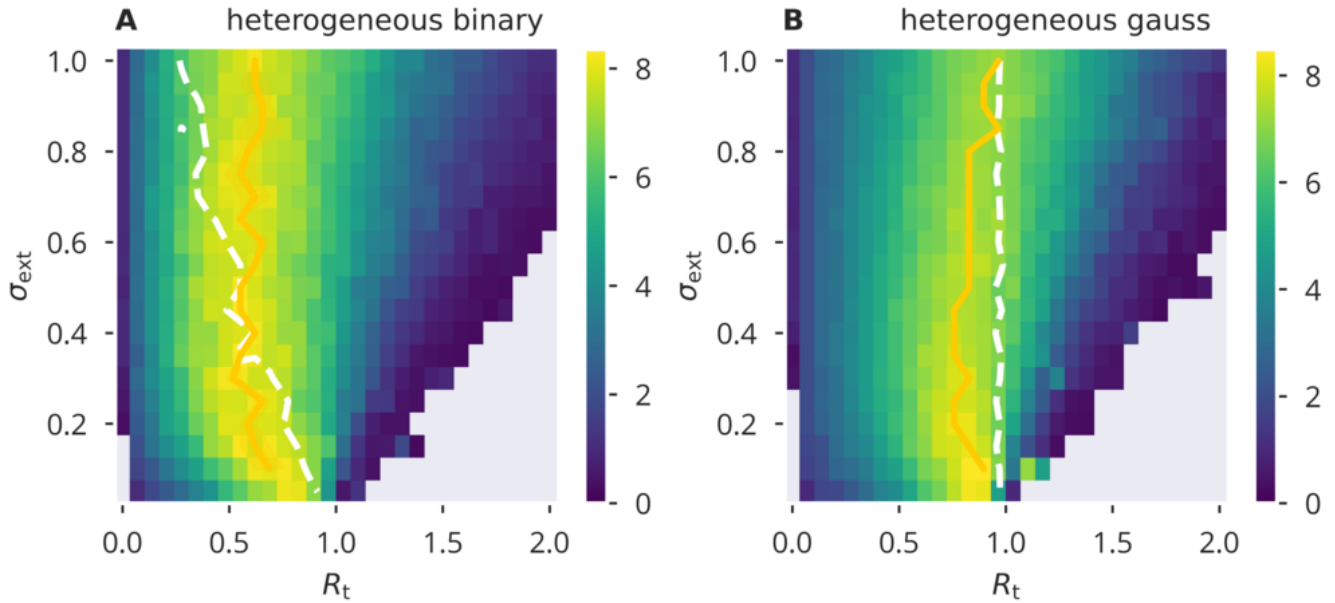


**Figure 3. XOR performance for flow control.** Color-coded performance sweeps for the XOR-performance (18) after adaptation using flow control. Averaged over five trials. The input has variance  $\sigma_{\text{ext}}^2$  and the target for the spectral radius is  $R_t$ . A/B panels are for heterogeneous binary/Gaussian input protocols. Optimal performance for a given  $\sigma_{\text{ext}}$  was estimated as a trial average (yellow solid line) and found to be generally close to criticality,  $R_a = 1$ , as measured (white dashed lines).

in Section 5.6. Assuming statistical independence across the population for  $y_i(t)$ , it is simply given by  $\sigma_{\text{bare}}^2 = \sigma_w^2 \sigma_y^2$ , where

$$\sigma_w^2 \equiv \text{Var} \left[ \sum_{j=1}^N W_{ij} \right] \tag{20}$$

is the variance of the sum of the bare afferent synaptic weights (see also Section 5.1). Being a crucial element of the proposed rules, deviations from the prediction of  $\sigma_{\text{bare}}^2$  would also negatively affect the precision of tuning the spectral radius. In Figure 5, a comparison of the deviations  $|\sigma_{\text{bare}}^2 - \sigma_w^2 \sigma_y^2|$  is presented for the four input protocols introduced in Section 5.3. For the Gaussian protocols, for which neurons receive statistically uncorrelated external signals, one observes that  $\sigma_{\text{bare}}^2 \rightarrow \sigma_w^2 \sigma_y^2$  in the thermodynamic limit  $N \rightarrow \infty$  via a power law, which is to be expected when the presynaptic neural activities are decorrelated. On the other side, binary 0/1 inputs act synchronous on all sites, either with site-dependent or site-independent strengths (heterogeneous/homogeneous). Corresponding activity correlations are induced and a finite and only weakly size-dependent difference between  $\sigma_{\text{bare}}^2$  and  $\sigma_w^2 \sigma_y^2$  shows up. Substantial corrections to the analytic theory are to be expected in this case. To this extend we measured the cross-correlation  $C(y_i, y_j)$ , defined as

$$\bar{C} = \frac{1}{N(N-1)} \sum_{i \neq j} |C(y_i, y_j)|, \quad C(y_i, y_j) = \frac{\text{Cov}(y_i, y_j)}{\sqrt{\text{Cov}(y_i, y_i) \text{Cov}(y_j, y_j)}}, \tag{21}$$

with the covariance given by  $\text{Cov}(y_i, y_j) = \langle (y_i - \langle y_i \rangle_t)(y_j - \langle y_j \rangle_t) \rangle_t$ . For a system of  $N = 500$  neurons the results for the averaged absolute correlation  $\bar{C}$  are presented in Figure 6 (see Figure 20 in the supplementary material for homogeneous input protocols). Autonomous echo-state layers are in chaotic states when supporting a finite activity level, which implies that correlations vanish in the thermodynamic

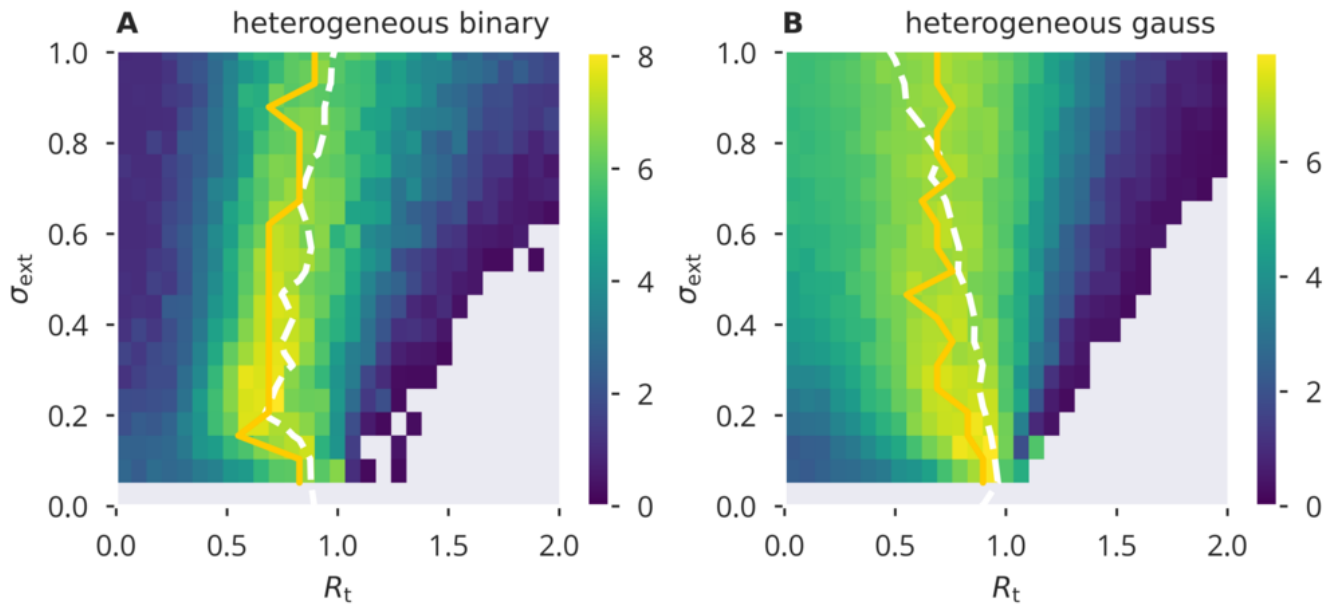


**Figure 4. XOR performance for variance control.** Color-coded performance sweeps for the XOR-performance (18) after adaptation using variance control. Averaged over five trials. The input has variance  $\sigma_{\text{ext}}^2$  and the target for the spectral radius  $R_t$ . A/B panels are for heterogeneous binary/Gaussian input protocols. Optimal performance (yellow solid line) is in general close to criticality,  $R_a = 1$ , as measured (white dashed lines).

limit  $N \rightarrow \infty$ . The case  $\sigma_{\text{ext}} = 0$ , as included in Figure 6, serves consequently as a yardstick for the magnitude of correlations that are due to the finite number of neurons.

Input correlations were substantially above the autonomous case for correlated binary inputs, with the magnitude of  $\bar{C}$  decreasing when the relative contribution of the recurrent activity increased. This was the case for increasing  $R_a$ . The effect was opposite for the Gaussian protocol, for which the input did not induce correlations, but contributed to decorrelating neural activity. In this case, the mean absolute correlation  $\bar{C}$  was suppressed when the internal activity became small in the limit  $R_a \rightarrow 0$ . For larger  $R_a$ , the recurrent input gained more impact on neural activity relative to the external drive and thus drove  $\bar{C}$  towards an amount of correlation that would be expected in the autonomous case.

### 3 DISCUSSION

The mechanisms for tuning the spectral radius via a local homeostatic adaptation rule introduced in the present study require neurons to have the ability to distinguish and locally measure both external and recurrent input contributions. For flow control, neurons need to be able to compare the recurrent membrane potential with their own activity, as assumed in Section 2.2. On the other hand, variance control directly measures the variance of the external input and derives the activity target variance accordingly. The limiting factor to a successful spectral radius control is the amount of cross-correlation induced by external driving statistics. As such, the functionality and validity of the proposed mechanisms depended on the ratio between external input, i.e. feed-forward or feedback connections, with respect to recurrent, or lateral connections. In general, it is not straightforward to directly connect experimental evidence regarding the ratio between recurrent and feed-forward contributions to the effects observed in the model. It is, however, worthwhile to note that the fraction of synapses associated with interlaminar loops and intralaminar lateral connections are estimated to make up roughly 50% (Binzegger et al., 2004). Relating this to our model, it implies that the significant interneural correlations that we observed when external input strengths were of the

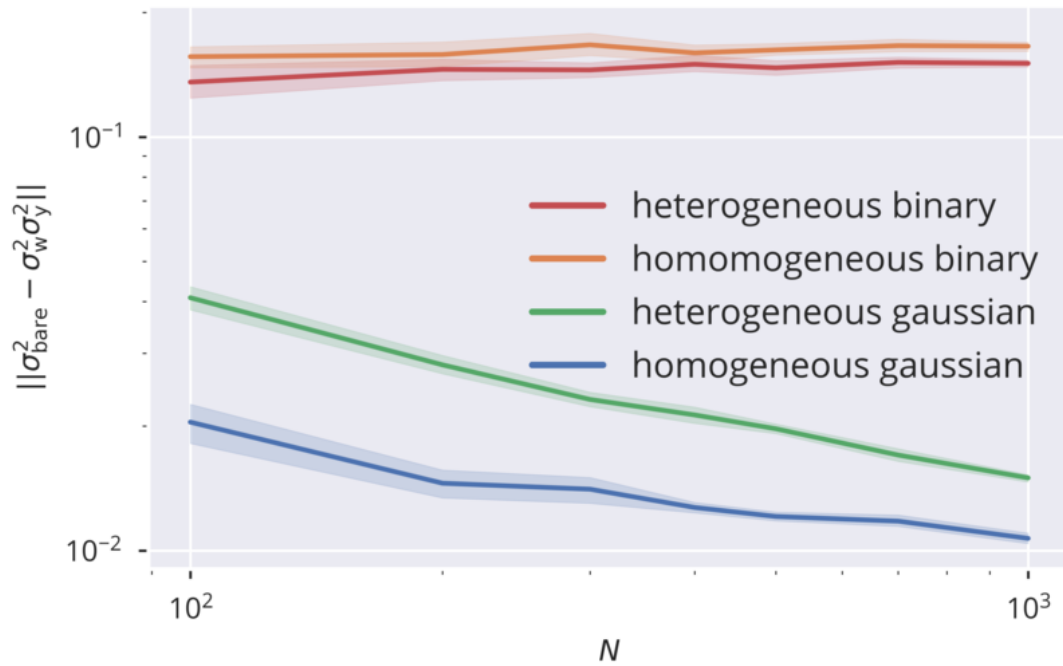


**Figure 5. Size dependence of correlation.** Comparison between the variance  $\sigma_{\text{bare}}^2$  of the bare recurrent input  $x_{\text{bare}} = \sum_j W_{ij} y_j$  with  $\sigma_w^2 \sigma_y^2$ . Equality is given when the presynaptic activities are statistically independent. This can be observed in the limit of large network sizes  $N$  for uncorrelated input data streams (homogeneous and heterogeneous Gaussian input protocols), but not for correlated inputs (homogeneous and heterogeneous binary input protocols). Compare Section 5.3 for the input protocols. Parameters are  $\sigma_{\text{ext}} = 0.5$ ,  $R_a = 1$  and  $\mu_t = 0.05$ .

same order of magnitude as the recurrent inputs, can not generally be considered an artifact of biologically implausible parameter choices. Synchronization (Echeveste and Gros, 2016) is in fact a widely observed phenomenon in the brain (Usrey and Reid, 1999), with possible relevance for information processing (Salinas and Sejnowski, 2001).

On the other hand, correlations due to shared input reduces the amount of information that can be stored in the neural ensemble (Bell and Sejnowski, 1995). Maximal information is achieved if neural activities or spikes trains form an orthogonal ensemble (Földiak, 1990; Bell and Sejnowski, 1995; Tetzlaff et al., 2012). Furthermore, neural firing in cortical microcircuits was found to be decorrelated across neurons, even if common external input was present (Ecker et al., 2010), that is, under a common orientation tuning. Therefore, the correlation we observed in our network due to shared input might be significantly reduced by possible modifications/extensions of our model: First, a strict separation between inhibitory and excitatory nodes according to Dale's law might help actively decorrelating neural activity (Tetzlaff et al., 2012; Bernacchia and Wang, 2013). Second, if higher dimensional input was used, a combination of plasticity mechanisms in the recurrent and feed-forward connections could lead to the formation of an orthogonal representation of the input (Földiak, 1990; Bell and Sejnowski, 1995; Wick et al., 2010), leading to richer, "higher dimensional" activity patterns, i. e. a less dominant largest principal component. Ultimately, if these measures helped in reducing neural cross-correlations in the model, we thus would expect them to also increase the accuracy of the presented adaptation mechanisms. We leave these modifications to possible future research.

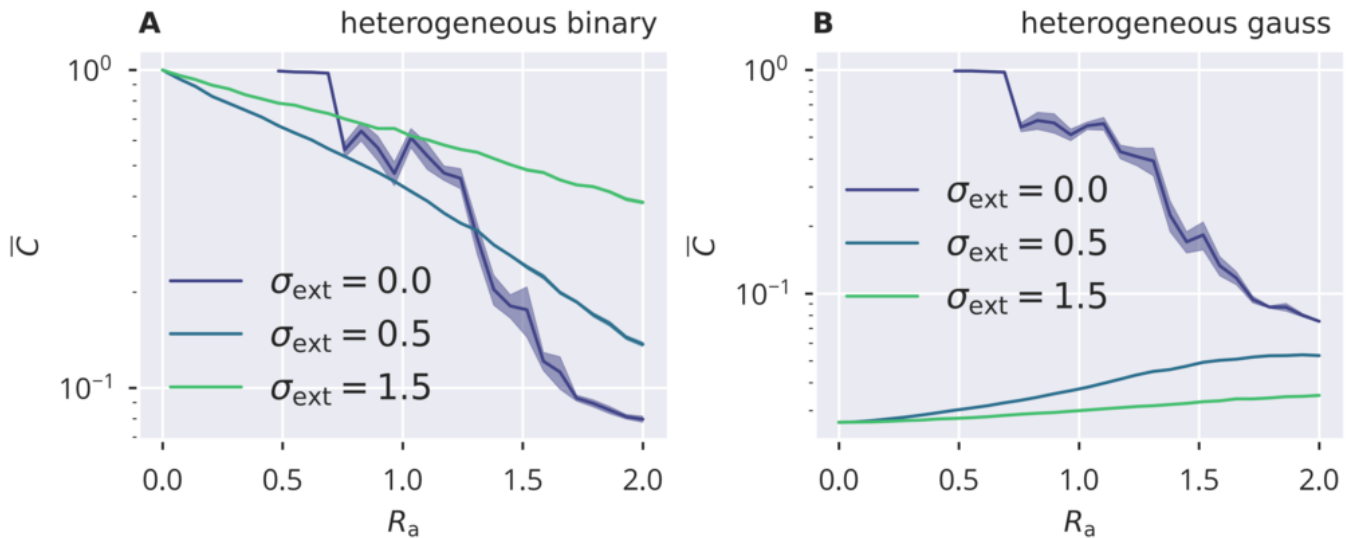


**Figure 6. Input induced activity correlations.** For heterogeneous binary and Gaussian inputs (A/B), the dependency of mean activity cross correlations  $\bar{C}$ , see Eq. (21).  $\bar{C}$  is shown as a function of the spectral radius  $R_a$ . Results are obtained for  $N = 500$  sites by averaging over five trials, with shadows indicating the standard error across trials. Correlations are due to finite-size effect for the autonomous case  $\sigma_{\text{ext}} = 0$ .

Overall, we found flow control to be generally more robust than variance control in the sense that, while still being affected by the amount of correlations within the neural reservoir, the task performance was less so prone to changes in the external input strength. Comparatively stable network performance could be observed, in spite of certain deviations from the desired spectral radius (see Figure 3). A possible explanation may be that flow control uses a distribution of samples from only a restricted part of phase space, that is, from the phase space regions that are actually visited or “used” for a given input. Therefore, while a spectral radius of unity ensures –statistically speaking– the desired scaling properties in all phase-space directions, it seem to be enough to control the correct scaling for the subspace of activities that is actually used for a given set of input patters. Variance control, on the other hand, relies more strictly on the assumptions that neural activities are statistical independent. In consequence, the desired results could only be achieved under a rather narrow set of input statistics (independent Gaussian input with small variance). In addition, the approximate expression derived for the nonlinear transformation appearing in the mean field approximation adds another layer of potential source of systematic error to the control mechanism. This aspect also speaks in favor of flow control, since its rules are mathematically more simple. In contrast to variance control, the stationarity condition stated in Eq. (12) is independent of the actual nonlinear activation function used and could easily be adopted in a modified neuron model. It should be noted, however, that the actual target  $R_t$  giving optimal performance might then also be affected.

Interestingly, flow control distinguishes itself from a conventional local activity-target perspective of synaptic homeostasis: There is no predefined set point in Eq. (5). This allows heterogeneities of variances of neural activity to develop across the network, while retaining the average neural activity at a fixed predefined level.

We would like to point out that, for all the results presented here, only stationary processes were used for generating the input sequences. Therefore, it might be worth considering the potential effects of non-stationary, yet bounded, inputs on the results in future work. It should be noted, however, that the temporal domain enters both adaptation mechanisms only in the form of trailing averages of first and second moments. As a consequence, we expect the issue of non-stationarity of external inputs to present itself

simply as a trade-off between slower adaptation, i.e. longer averaging time scales, and the mitigation of the effects of non-stationarities. Slow adaptation is, however, completely in line with experimental results on the dynamics of synaptic scaling, which is taking place on the time scale of hours to days (Turrigiano et al., 1998; Turrigiano, 2008).

## 4 CONCLUSION

Apart from being relevant from a theoretical perspective, we propose that the separability of recurrent and external contributions to the membrane potential is an aspect that is potentially relevant for the understanding of local homeostasis in biological networks. While homeostasis in neural compartments has been a subject of experimental research (Chen et al., 2008), to our knowledge, it has not yet been further investigated on a theoretical basis, although it has been hypothesized that the functional segregation within the dendritic structure might also affect (among other intraneural dynamical processes) homeostasis (Narayanan and Johnston, 2012). The neural network model used in this study lacks certain features characterizing biological neural networks, like strict positivity of the neural firing rate or Dale's law, viz E-I balance (Trapp et al., 2018). Future research should therefore investigate whether the here presented framework of local flow control can be implemented within more realistic biological neural network models. A particular concern regarding our findings is that biological neurons are spiking. The concept of an underlying instantaneous firing rate is, strictly speaking, a theoretical construct, let alone the definition of higher moments, such as the "variance of neural activity". It is however acknowledged that the variability of the neural activity is central for statistical inference (Echeveste et al., 2020). It is also important to note that real-world biological control mechanisms, e.g. of the activity, rely on physical quantities that serve as measurable correlates. A well-known example is the intracellular calcium concentration, which is essentially a linearly filtered version of the neural spike train (Turrigiano, 2008). On a theoretical level, Cannon and Miller showed that dual homeostasis can successfully control the mean and variance of this type of spike-averaging physical quantities (Cannon and Miller, 2017). An extension of the flow control to filtered spike trains of spiking neurons could be an interesting subject of further investigations. However, using spiking neuron models would have shifted the focus of our research towards the theory of liquid state machines (Maass et al., 2002; Maass and Markram, 2004), exceeding the scope of this publication. We therefore leave the extension to more realistic network/neuron models to future work.

## 5 MATERIALS AND METHODS

### 5.1 Model

We implemented an echo state network with  $N$  neurons, receiving  $D_{\text{in}}$  inputs. The neural activity is  $y_i \in [-1, 1]$ ,  $x_i$  the membrane potential,  $u_i$  the input activities,  $W_{ij}$  the internal synaptic weights and  $I_i$  the external input received. The output layer will be specified later. The dynamics

$$x_i(t) = a_i \sum_{j=1}^N W_{ij} y_j(t-1) + I_i(t), \quad y_i(t) = \tanh(x_i(t) - b_i) \quad (22)$$

is discrete in time, where the input  $I_i$  is treated instantaneously. A tanh-sigmoidal has been used as a nonlinear activation function.

The synaptic renormalization factor  $a_i$  in (22) can be thought of as a synaptic scaling parameter that neurons use to regulate the overall strength of the recurrent inputs. The strength of the inputs  $I_i$  is unaffected,

which is biologically plausible if external and recurrent signals arrive at separate branches of the dendritic tree (Spruston, 2008).

The  $W_{ij}$  are the bare synaptic weights, with  $a_i W_{ij}$  being the components of the effective weight matrix  $\widehat{W}_a$ . Key to our approach is that the propagation of activity is determined by  $\widehat{W}_a$ , which implies that the spectral radius of the effective, and not of the bare weight matrix needs to be regulated.

The bare synaptic matrix  $W_{ij}$  is sparse, with a connection probability  $p_r = 0.1$ . The non-zero elements are drawn from a Gaussian with standard deviation

$$\sigma = \frac{\sigma_w}{\sqrt{N p_r}}, \quad (23)$$

and vanishing mean  $\mu$ . Here  $N p_r$  corresponds to the mean number of afferent internal synapses, with the scaling  $\sim 1/\sqrt{N p_r}$  enforcing size-consistent synaptic-weight variances. As discussed in the results section, we applied the following adaptation mechanisms:

$$b_i(t) = b_i(t-1) + \epsilon_b [y_i(t) - \mu_t] \quad (24)$$

for the thresholds  $b_i$ .

- Adaption of gains, using flow control:

$$a_i(t) = a_i(t-1) \left[ 1 + \epsilon_a \Delta R_i(t) \right], \quad \Delta R_i(t) = R_t^2 |y_i(t-1)|^2 - |x_{r,i}(t)|^2. \quad (25)$$

- Adaption of gains, with variance control:

$$a_i(t) = a_i(t-1) + \epsilon_a \left[ \sigma_{t,i}^2(t) - (y_i(t) - \mu_i^y(t))^2 \right] \quad (26)$$

$$\sigma_{t,i}^2(t) = 1 - \sqrt{1 + 2R_t^2 y_i(t)^2 + 2\sigma_{\text{ext},i}^2(t)} \quad (27)$$

$$\mu_i^y(t) = \mu_i^y(t-1) + \epsilon_\mu [y_i(t) - \mu_i^y(t-1)] \quad (28)$$

$$\sigma_{\text{ext},i}^2(t) = \sigma_{\text{ext},i}^2(t-1) + \epsilon_\sigma \left[ (I_i(t) - \mu_{\text{ext},i}(t))^2 - \sigma_{\text{ext},i}^2(t-1) \right] \quad (29)$$

$$\mu_{\text{ext},i}(t) = \mu_{\text{ext},i}(t-1) + \epsilon_\mu [I_i(t) - \mu_{\text{ext},i}(t-1)] \quad (30)$$

Note that Eq. (28)–(30) have the same mathematical form

$$\langle \text{trail} \rangle(t) = \langle \text{trail} \rangle(t-1) + \epsilon [\langle \text{var} \rangle(t) - \langle \text{trail} \rangle(t-1)]$$

since they only serve as trailing averages that are used in the two main equation (26) and (27).

For a summary of all model parameters, see Table 1.

**Table 1.** Standard values for model parameters

$N$	$p_r$	$\sigma_w$	$\mu_t$	$\epsilon_b$	$\epsilon_a$	$\epsilon_\mu$	$\epsilon_\sigma$
500	0.1	1	0.05	$10^{-3}$	$10^{-3}$	$10^{-4}$	$10^{-3}$



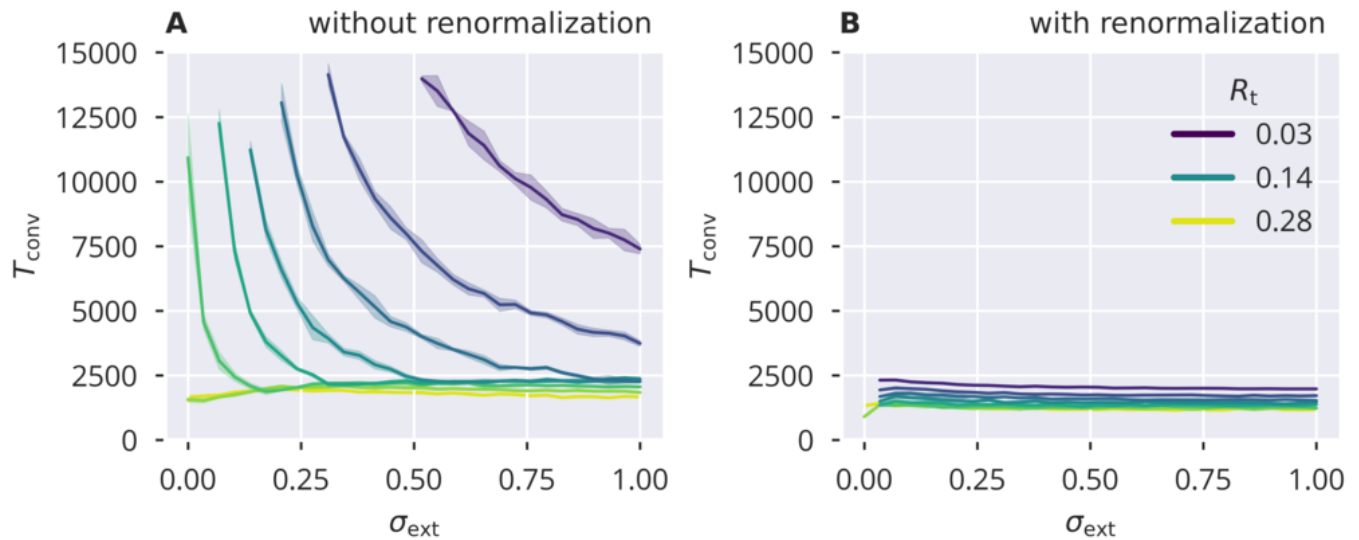


**Figure 7. Convergence time with and without adaptation rate renormalization** Number of time steps  $T_{\text{conv}}$  needed for  $|R_a(t) - R_a(t - 1)|^2$  to fall below  $10^{-3}$ . Shown are results using heterogeneous Gaussian input without and with, (A) and respectively (B), a renormalization of the learning rate  $\epsilon_a \rightarrow \epsilon_a/\bar{x}_r^2$ . Note that, due to computational complexity, an estimate of  $R_a$  given by (10) was used. An initial offset of 0.5 from the target  $\bar{R}_t$  was used for all runs. Color coding of  $R_t$  is the same in both panels.

### 5.2 Convergence acceleration for flow control

For small values of  $R_t$  and weak external input, the average square activities and membrane potentials  $y_i^2(t)$  and  $x_{i,i}^2(t)$  can become very small. As a consequence, their difference entering  $\Delta R_i(t)$  in (25) also becomes small in absolute value, slowing down the convergence process. To eliminate this effect, we decided to rescale the learning rate by a trailing average of the squared recurrent membrane potential, i. e.  $\epsilon_a \rightarrow \epsilon_a/\bar{x}_r^2$ . The effect of this renormalization is shown in Fig. 7. Rescaling the learning rate effectively removes the significant rise of convergence times for small  $\sigma_{\text{ext}}$  and small  $R_t$ .

### 5.3 Input protocols

Overall, we examined four distinct input protocols.

- *Homogeneous Gaussian.* Nodes receive inputs  $I_i(t)$  that are drawn individually from a Gaussian with vanishing mean and standard deviation  $\sigma_{\text{ext}}$ .
- *Heterogeneous Gaussian.* Nodes receive stochastically independent inputs  $I_i(t)$  that are drawn from Gaussian distributions with vanishing mean and node specific standard deviations  $\sigma_{i,\text{ext}}$ . The individual  $\sigma_{i,\text{ext}}$  are normal distributed, as drawn from the positive part of a Gaussian with mean zero and variance  $\sigma_{\text{ext}}^2$ .
- *Homogeneous binary.* Sites receive identical inputs  $I_i(t) = \sigma_{\text{ext}}u(t)$ , where  $u(t) = \pm 1$  is a binary input sequence.
- *Heterogeneous binary.* We define with

$$I_i = W_i^u u(t), \quad u_j(t) = \pm 1 \tag{31}$$

the afferent synaptic weight vector  $W_i^u$ , which connects the binary input sequence  $u(t)$  to the network. All  $W_i^u$  are drawn independently from a Gaussian with mean zero and standard deviation  $\sigma_{\text{ext}}$ .

The Gaussian input variant simulates external noise. We used it in particular to test predictions of the theory developed in Section 5.6. In order to test the performance of the echo state network with respect to the delayed XOR task, the binary input protocols are employed. A generalization of the here defined protocols to the case of higher-dimensional input signals would be straightforward.

#### 5.4 Spectral radius adaptation dynamics

For an understanding of the spectral radius adaptation dynamics of flow control, it is of interest to examine the effect of using the global adaptation constraint

$$\Delta R_i(t) = \frac{1}{N} \left[ R_t^2 \|\mathbf{y}(t-1)\|^2 - \|\mathbf{x}_r(t)\|^2 \right] \quad (32)$$

in (5). The spectral radius condition (12) is then enforced directly, with the consequence that (32) is stable and precise even in the presence of correlated neural activities (see Figure 1C). This rule, while not biologically plausible, provides an opportunity to examine the dynamical flow, besides the resulting state. There are two dynamic variables,  $a = a_i \forall i$ , where, for the sake of simplicity, we assumed that all  $a_i$  are homogeneous, and the activity variance  $\sigma_y^2 = \|\mathbf{y}\|^2/N$ . The evolution of  $(a, \sigma_y^2)$  resulting from the global rule (6) is shown in Figure 8. For the flow,  $\Delta a = a(t+1) - a(t)$  and  $\Delta \sigma_y^2 = \sigma_y^2(t) - \sigma_y^2(t-1)$ , the approximation

$$\Delta a = \epsilon_a a (R_t^2 - a^2 \sigma_w^2) \sigma_y^2 \quad (33)$$

$$\Delta \sigma_y^2 = 1 - \sigma_y^2 - \frac{1}{\sqrt{1 + 2a^2 \sigma_w^2 \sigma_y^2 + 2\sigma_{\text{ext}}}} \quad (34)$$

is obtained. For the scaling factor  $a$ , this leads to a fixed point of  $R_t/\sigma_w$ . We used the mean-field approximation for neural variances that is derived in Section 5.6. The analytic flow compares well with numerics, as shown in Figure 8. For a subcritical rescaling factor  $a$  and  $\sigma_{\text{ext}} = 0$ , the system flows towards a line of fixpoints defined by a vanishing  $\sigma_y^2$  and a finite  $a \in [0, 1]$ , see Figure 8A. When starting with  $a > 0$ , the fixpoint is instead  $(a, \sigma_y^2) = (1, 0)$ . The situation changes qualitatively for finite external inputs, viz when  $\sigma_{\text{ext}} > 0$ , as shown in Figure 8B–D. The nullcline  $\Delta \sigma_y^2 = 0$  is now continuous and the system flows to the fixed point, as shown in Figure 8B–D, with the value of  $\sigma_y^2$  being determined by the intersection of the two nullclines. In addition, we also varied the target spectral radius, see Figure 8B/C. This caused a slight mismatch between the flow of the simulated systems and the analytic flow. It should be noted, however, that this is to be expected anyhow since we used an approximation for the neural variances, again, see Section 5.6.

This analysis shows that external input is necessary for a robust flow towards the desired spectral weight, the reason being that the dynamics dies out before the spectral weight can be adapted when the isolated systems starts in the subcritical regime.

#### 5.5 Extended theory of flow control for independent neural activity

We would like to show that the stationarity condition in Eq. (12) results in the correct spectral radius, under the special case of independently identically distributed neural activities with zero mean.

We start with Eq. (12) as a stationarity condition for a given  $R_t$ :

$$\langle \|\mathbf{x}_r(t)\|^2 \rangle_t \stackrel{!}{=} R_t^2 \langle \|\mathbf{y}(t-1)\|^2 \rangle_t. \quad (35)$$

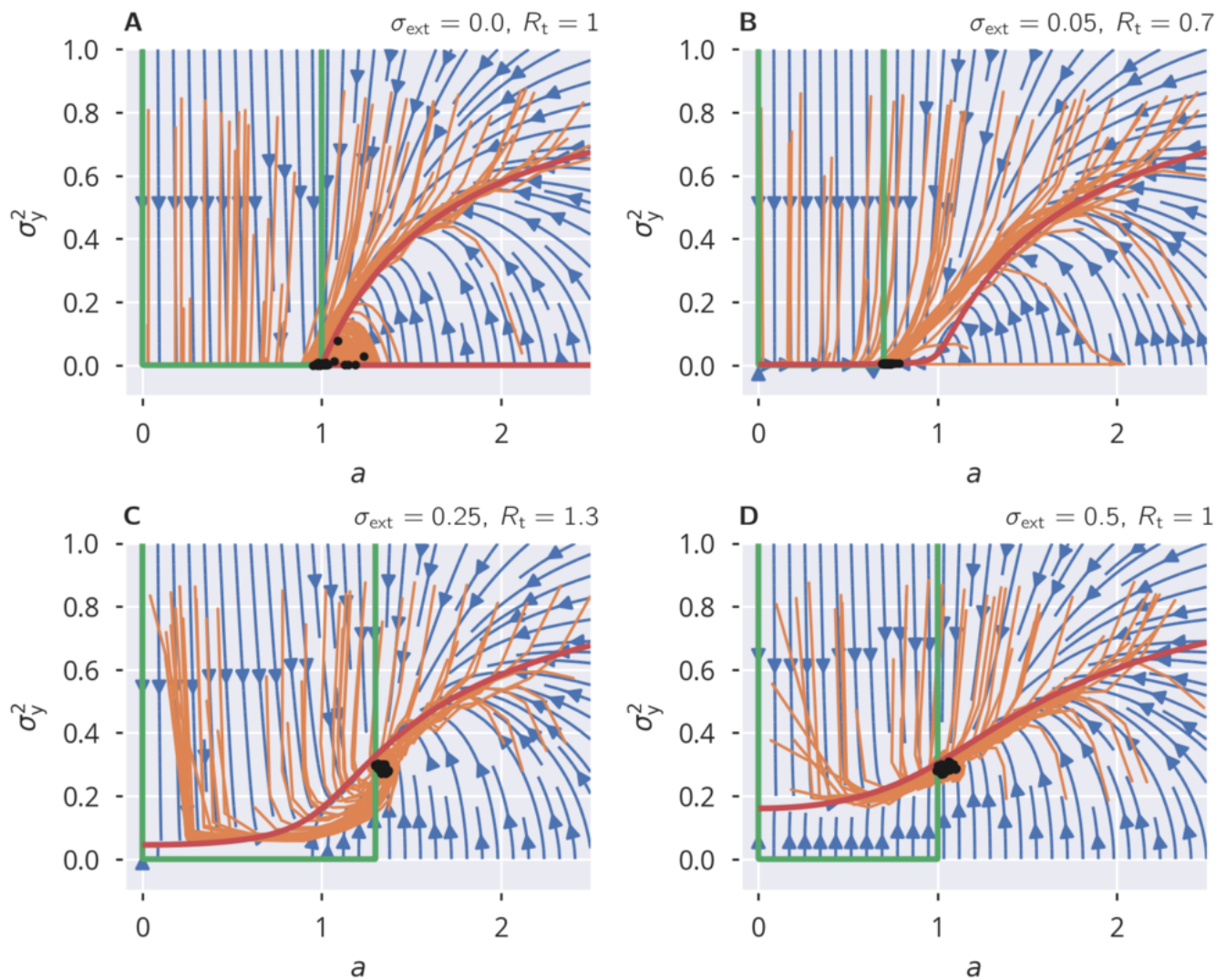


**Figure 8. Spectral radius adaptation dynamics.** The dynamics of the synaptic rescaling factor  $a$  and the squared activity  $\sigma_y^2$  (orange), as given by (6), for  $R_t = 1$ . Also shown is the analytic approximation to the flow (blue), see (33) and (34), and the respective nullclines  $\Delta a = 0$  (green) and  $\Delta \sigma_y^2 = 0$  (red). For the input, the heterogeneous binary protocol is used. Panels **A** to **D** correspond to different combinations of external input strengths and target spectral radii. The black dots show the steady-state configurations of the simulated systems.  $\epsilon_a = 0.1$ .

We can express the left side of the equation as

$$E \left[ \mathbf{y}^\dagger(t) \widehat{W}_a^\dagger \widehat{W}_a \mathbf{y}(t) \right]_t. \tag{36}$$

We define  $\widehat{U}_a \equiv \widehat{W}_a^\dagger \widehat{W}_a$  with  $\{\sigma_k^2\}$  being the set of eigenvalues, which are also the squared singular values of  $\widehat{W}_a$ , and  $\{\mathbf{u}_k\}$  the respective set of orthonormal (column) eigenvectors. We insert the identity

$\sum_{k=1}^N \mathbf{u}_k \mathbf{u}_k^\dagger$  and find

$$\mathbb{E} \left[ \mathbf{y}^\dagger(t) \widehat{U}_a \sum_{k=1}^N \mathbf{u}_k \mathbf{u}_k^\dagger \mathbf{y}(t) \right]_t \quad (37)$$

$$= \mathbb{E} \left[ \sum_{k=1}^N \sigma_k^2 \mathbf{y}^\dagger(t) \mathbf{u}_k \mathbf{u}_k^\dagger \mathbf{y}(t) \right]_t \quad (38)$$

$$= \sum_{k=1}^N \sigma_k^2 \mathbf{u}_k^\dagger \mathbb{E} \left[ \mathbf{y}(t) \mathbf{y}^\dagger(t) \right]_t \mathbf{u}_k \quad (39)$$

$$= \sum_{k=1}^N \sigma_k^2 \mathbf{u}_k^\dagger \widehat{C}_{yy} \mathbf{u}_k \quad (40)$$

$$= \text{Tr} \left( \widehat{D}_{\sigma^2} \widehat{S}_u^\dagger \widehat{C}_{yy} \widehat{S}_u \right). \quad (41)$$

Given zero mean neural activity,  $\widehat{C}_{yy} = \mathbb{E}[\mathbf{y}(t) \mathbf{y}^\dagger(t)]_t$  is the covariance matrix of neural activities.  $\widehat{D}_{\sigma^2}$  is a diagonal matrix holding the  $\{\sigma_k^2\}$  and  $\widehat{S}_u$  is a unitary matrix whose columns are  $\{\mathbf{u}_k\}$ .  $\widehat{S}_u^\dagger \widehat{C}_{yy} \widehat{S}_u$  is expressing  $\widehat{C}_{yy}$  in the diagonal basis of  $\widehat{U}_a$ .

Including the right hand side of (35), we get

$$\text{Tr} \left( \widehat{D}_{\sigma^2} \widehat{S}_u^\dagger \widehat{C}_{yy} \widehat{S}_u \right) = R_t^2 \text{Tr} \left( \widehat{C}_{yy} \right). \quad (42)$$

However, since the trace is invariant under a change of basis, we find

$$\text{Tr} \left( \widehat{D}_{\sigma^2} \widehat{S}_u^\dagger \widehat{C}_{yy} \widehat{S}_u \right) = R_t^2 \text{Tr} \left( \widehat{S}_u^\dagger \widehat{C}_{yy} \widehat{S}_u \right). \quad (43)$$

Defining  $\widehat{C}^u \equiv \widehat{S}_u^\dagger \widehat{C}_{yy} \widehat{S}_u$ , we get

$$\sum_{k=1}^N \sigma_k^2 C_{kk}^u = R_t^2 \sum_{k=1}^N C_{kk}^u. \quad (44)$$

If we assume that the node activities are independently identically distributed with zero mean, we get  $(\widehat{C}_{yy})_{ij} = (\widehat{C}^u)_{ij} = \langle y^2 \rangle_t \delta_{ij}$ . In this case, which was also laid out in Section 2.6, the equation reduces to

$$\sum_{k=1}^N \sigma_k^2 = R_t^2 N. \quad (45)$$

The Frobenius norm of a square Matrix  $\widehat{A}$  is given by  $\|\widehat{A}\|_F^2 \equiv \sum_{i,j} \widehat{A}_{ij}^2$ . Furthermore, the Frobenius norm is linked to the singular values via  $\|\widehat{A}\|_F^2 = \sum_k \sigma_k^2(\widehat{A})$  (Sengupta and Mitra, 1999; Shen, 2001). This allows us to state

$$\sum_{i,j} \left( \widehat{W}_a \right)_{ij}^2 = R_t^2 N \quad (46)$$

which, by using (10), gives

$$R_a^2 = R_t^2. \tag{47}$$

A slightly less restrictive case is that of uncorrelated but inhomogeneous activity, that is  $(\widehat{C}_{yy})_{ij} = \langle y_i^2 \rangle_t \delta_{ij}$ . The statistical properties of the diagonal elements  $C_{kk}^u$  then determine to which degree one can still claim that Eq. (44) leads to Eq. (45). Figure 21 in the supplementary materials shows an example of a randomly generated realization of  $(\widehat{C}_{yy})_{ij} = \langle y_i^2 \rangle_t$  and the resulting diagonal elements of  $\widehat{C}^u$ , where the corresponding orthonormal basis  $\widehat{S}_u$  was generated from the SVD of a random Gaussian matrix. As one can see, the basis transformation has a strong smoothing effect on the diagonal entries, while the mean over the diagonal elements is preserved. Note that this effect was not disturbed by introducing random row-wise multiplications to the random matrix from which the orthonormal basis was derived. The smoothing of the diagonal entries allows us to state that  $C_{kk}^u \approx \langle y^2 \rangle$  is a very good approximation in the case considered, which therefore reduces (44) to the homogeneous case previously described. We can conclude that the adaptation mechanism also gives the desired spectral radius under uncorrelated inhomogeneous activity.

In the most general case, we can still state that if  $C_{kk}^u$  and  $\sigma_k^2$  are uncorrelated, for large  $N$ , Eq. (44) will tend towards

$$N \langle \sigma^2 \rangle \langle C^u \rangle = NR_t^2 \langle C^u \rangle \tag{48}$$

which would also lead to Eq. (45). However, we can not generally guarantee statistical independence since the recurrent contribution on neural activities and the resulting entries of  $\widehat{C}_{yy}$  and thus also  $C_{kk}^u$  are linked to  $\widehat{S}$  and  $\sigma_k^2$ , being the SVD of the recurrent weight matrix.

### 5.6 Mean field theory for echo state layers

In the following, we deduce analytic expressions allowing to examine the state of echo-state layers subject to a continuous timeline of inputs. Our approach is similar to the one presented by Massar and Massar (2013).

The recurrent part of the input  $x_i$  received by a neuron is a superposition of  $Np_t$  terms, which are assumed here to be uncorrelated. Given this assumption, the self-consistency equations

$$\sigma_{y,i}^2 = \int_{-\infty}^{\infty} dx \tanh^2(x) N_{\mu_i, \sigma_i}(x) - \mu_{y,i}^2 \tag{49}$$

$$\mu_{y,i} = \int_{-\infty}^{\infty} dx \tanh(x) N_{\mu_i, \sigma_i}(x) \tag{50}$$

$$\sigma_i^2 = a_i^2 \sigma_w^2 \langle \sigma_{y,j}^2 \rangle_j + \sigma_{\text{ext},i}^2, \quad \mu_i = \mu_{\text{ext},i} - b_i \tag{51}$$

determine the properties of the stationary state. We recall that  $\sigma_w$  parameterizes the distribution of bare synaptic weights via (23). The general expressions (49) and (50) hold for all neurons, with the site-dependency entering exclusively via  $a_i, b_i, \sigma_{\text{ext},i}$  and  $\mu_{\text{ext},i}$ , as in (51), with the latter characterizing the standard deviation and the mean of the input. Here,  $a_i^2 \sigma_w^2 \sigma_y^2$  is the variance of the recurrent contribution to the membrane potential,  $x$ , and  $\sigma^2$  the respective total variance. The membrane potential is Gaussian distributed, as  $N_{\mu, \sigma}(x)$ , with mean  $\mu$  and variance  $\sigma^2$ , which are both to be determined self-consistently. Variances are additive for stochastically independent processes, which has been assumed in (51) to be the case for recurrent activities and the external inputs. The average value for the mean neural activity is  $\mu_i$ .

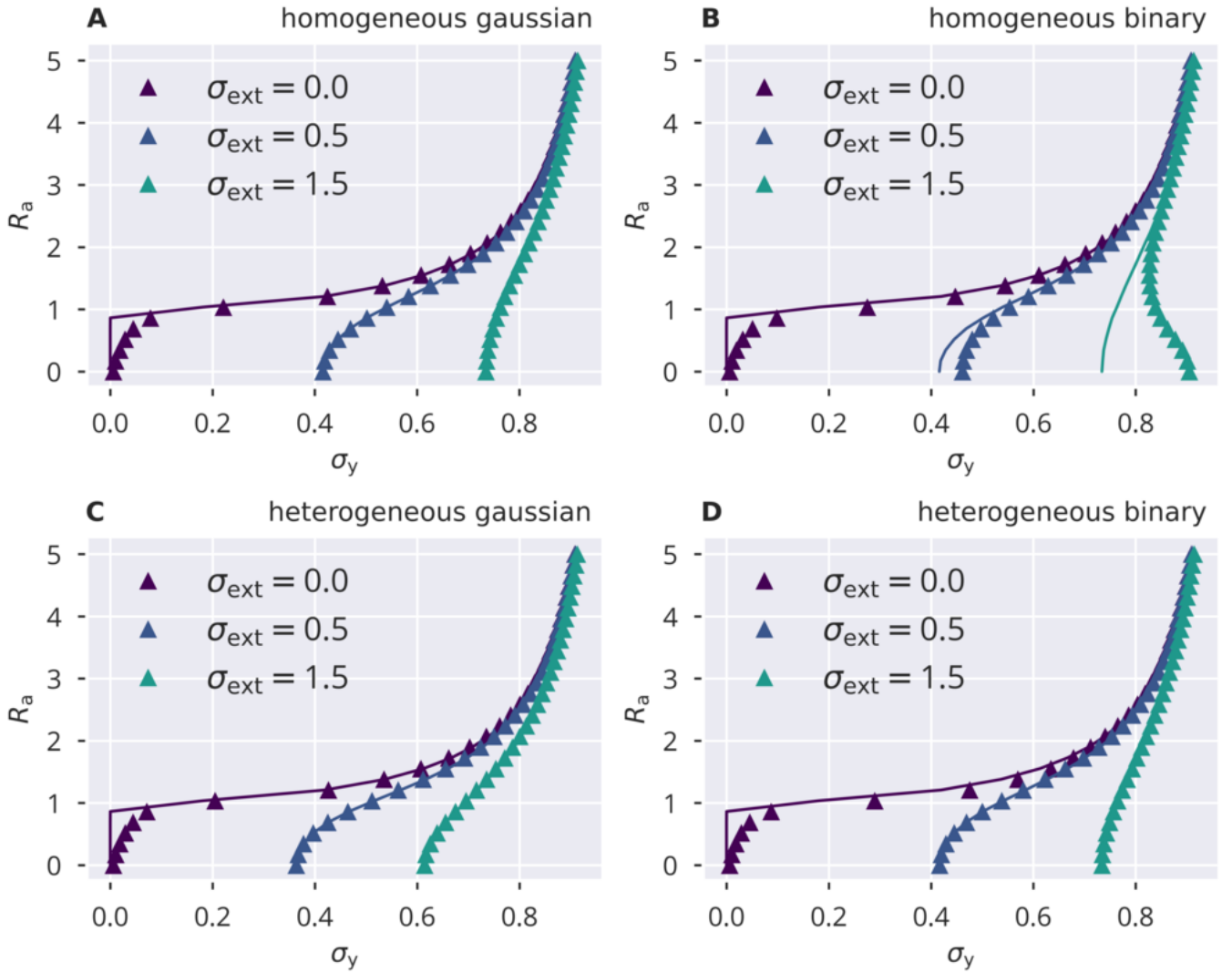


**Figure 9. Variance control for the spectral radius.** The spectral radius  $R_a$ , given by the approximation  $R_a^2 = \sum_i a_i^2/N$ , for the four input protocols defined in Section 5.3. Lines show the numerical self-consistency solution of (49), symbols the full network simulations. Note the instability for small  $\sigma_y$  and  $\sigma_{\text{ext}}$ . **A:** Homogeneous independent Gaussian input. **B:** Homogeneous identical binary input. **C:** Heterogeneous independent Gaussian input. **D:** Heterogeneous identical binary input.

For a given set of  $a_i$ ,  $\sigma_{\text{ext},i}$  and  $b_i$ , the means and variances of neural activities,  $\sigma_{y,i}^2$  and  $\mu_{y,i}$ , follow implicitly.

We compared the numerically determined solutions of (49) and (50) against full network simulations using, as throughout this study,  $N = 500$ ,  $p_r = 0.1$ ,  $\sigma_w = 1$ ,  $\mu_t = 0.05$ . In Figure 9, the spectral radius  $R_a$  is given for the four input protocols defined in Section 5.3. The identical ensemble of input standard deviations  $\sigma_{\text{ext},i}$  enters both theory and simulations. Theory and simulations are in good accordance for vanishing input. Here, the reason is that finite activity levels are sustained in an autonomous random neural network when the ongoing dynamics is chaotic and hence decorrelated. For reduced activity levels, viz for small variances  $\sigma_y^2$ , the convergence of the network dynamics is comparatively slow, which leads to a certain discrepancy with the analytic prediction (see Figure 9).

### 5.6.1 Gaussian approximation

The integral occurring in the self-consistency condition (49) can be evaluated explicitly when a tractable approximation to the squared transfer function  $\tanh^2(\cdot)$  is available. A polynomial approximation would capture the leading behavior close to the origin, however without accounting for the fact that  $\tanh^2(\cdot)$  converges to unity for large absolute values of the membrane potential. Alternatively, an approximation incorporating both conditions, the correct second-order scaling for small, and the correct convergence for large arguments, is given by the Gaussian approximation

$$\tanh^2(x) \approx 1 - \exp(-x^2) . \tag{52}$$

With this approximation the integral in (49) can be evaluated explicitly. The result is

$$\begin{aligned} \frac{1}{1 - \sigma_y^2 - \mu_y^2} &= \sqrt{1 + 2\sigma^2} / \exp(-\mu^2 / (1 + 2\sigma^2)) \\ &= \sqrt{1 + 2a^2\sigma_w^2\sigma_y^2 + 2\sigma_{\text{ext}}^2} / \exp(-\mu^2 / (1 + 2a^2\sigma_w^2\sigma_y^2 + 2\sigma_{\text{ext}}^2)) . \end{aligned} \tag{53}$$

Assuming that  $\mu \approx 0$  and  $\mu_y \approx 0$ , inverting the first equation yields a relatively simple analytic approximation for the variance self-consistency equation:

$$\sigma_y^2 = 1 - \frac{1}{\sqrt{1 + 2a^2\sigma_w^2\sigma_y^2 + 2\sigma_{\text{ext}}^2}} . \tag{54}$$

This equation was then used for the approximate update rule in (8) and (34).

Alternatively, we can write (54) as a self-consistency equation between  $\sigma_y^2, \sigma_{\text{ext}}^2, a^2\sigma_w^2 = R_a^2$ , describing a phase transition at  $R_a = 1$ :

$$2R_a^2\sigma_y^2 (1 - \sigma_y^2)^2 = 1 - (1 + 2\sigma_{\text{ext}}^2) (1 - \sigma_y^2)^2 . \tag{55}$$

See Fig. 10 for solutions of (55) for different values of  $\sigma_{\text{ext}}^2$ . Note that for vanishing external driving and values of  $R_a$  above but close to the critical point, the standard deviation  $\sigma_y$  scales with  $\sigma_y \propto (R_a - 1)^{1/2}$ , which is the typical critical exponent for the order parameter in classical Landau theory of second-order phase transitions (Gros, 2008, p. 169). If combined with a slow homeostatic process, flow or variance control in our case, this constitutes a system with an absorbing phase transition (Gros, 2008, p. 182-183), settling at the critical point  $R_a = 1$ . This phase transition can also be observed in Fig. 9 for  $\sigma_{\text{ext}} = 0$  as a sharp onset in  $\sigma_y$ .

### CONFLICT OF INTEREST STATEMENT

The authors declare that the research was conducted in the absence of any commercial or financial relationships that could be construed as a potential conflict of interest.

### AUTHOR CONTRIBUTIONS

Both authors, F.S. and C.G., contributed equally to the writing and review of the manuscript. F.S. provided the code, ran the simulations and prepared the figures.

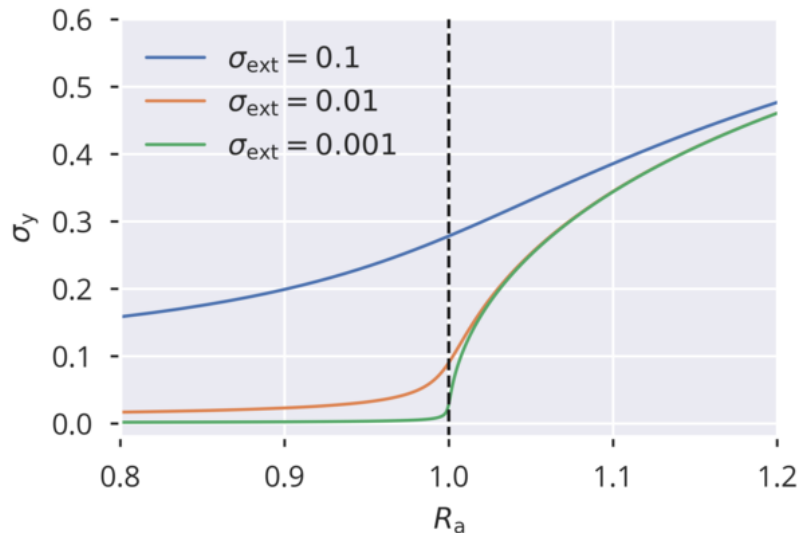


**Figure 10. Phase transition of activity variance** Shown are solutions of the analytical approximation given in (55), capturing the onset of activity (characterized by its variance  $\sigma_y^2$ ) at the critical point  $R_a = 1$ .

## ACKNOWLEDGMENTS

The authors acknowledge the financial support of the German research foundation (DFG) and discussions with R. Echeveste. This manuscript was published as a pre-print on biorxiv (Schubert and Gros, 2020).

## DATA AVAILABILITY STATEMENT

The datasets generated for this study can be found in [https://itp.uni-frankfurt.de/~fschubert/data\\_esn\\_frontiers/](https://itp.uni-frankfurt.de/~fschubert/data_esn_frontiers/).

Simulation and plotting code is available in [https://github.com/FabianSchubert/ESN\\_Frontiers](https://github.com/FabianSchubert/ESN_Frontiers).

## REFERENCES

- Abbott, L. F. and LeMasson, G. (1993). Analysis of Neuron Models with Dynamically Regulated Conductances. *Neural Computation* 5, 823–842. doi:10.1162/neco.1993.5.6.823
- Barral, J. and D’Reyes, A. (2016). Synaptic scaling rule preserves excitatory-inhibitory balance and salient neuronal network dynamics. *Nature Neuroscience* 19, 1690–1696. doi:10.1038/nn.4415
- Bell, A. J. and Sejnowski, T. J. (1995). An Information-maximisation approach to blind separation and blind deconvolution. *Neural Computation* 7, 1129–1159
- [Dataset] Bernacchia, A. and Wang, X. J. (2013). Decorrelation by recurrent inhibition in heterogeneous neural circuits. doi:10.1162/NECO\_a\_00451
- Binzegger, T., Douglas, R. J., and Martin, K. A. (2004). A quantitative map of the circuit of cat primary visual cortex. *Journal of Neuroscience* 24, 8441–8453. doi:10.1523/JNEUROSCI.1400-04.2004
- Boedeker, J., Obst, O., Mayer, N. M., and Asada, M. (2009). Initialization and self-organized optimization of recurrent neural network connectivity. *HFSP Journal* 3, 340–349. doi:10.2976/1.3240502
- Borde, M., Cazalets, J. R., and Buno, W. (1995). Activity-dependent response depression in rat hippocampal CA1 pyramidal neurons in vitro. *Journal of Neurophysiology* 74, 1714–1729. doi:10.1152/jn.1995.74.4.1714



- Cannon, J. and Miller, P. (2017). Stable Control of Firing Rate Mean and Variance by Dual Homeostatic Mechanisms. *Journal of Mathematical Neuroscience* 7. doi:10.1186/s13408-017-0043-7
- Chen, N., Chen, X., and Wang, J. H. (2008). Homeostasis established by coordination of subcellular compartment plasticity improves spike encoding. *Journal of Cell Science* 121, 2961–2971. doi:10.1242/jcs.022368
- Echeveste, R., Aitchison, L., Hennequin, G., and Lengyel, M. (2020). Cortical-like dynamics in recurrent circuits optimized for sampling-based probabilistic inference. *Nature Neuroscience* , 1138–1149
- Echeveste, R. and Gros, C. (2016). Drifting states and synchronization induced chaos in autonomous networks of excitable neurons. *Frontiers in computational neuroscience* 10, 98
- Ecker, A. S., Berens, P., Keliris, G. A., Bethge, M., Logothetis, N. K., and Tolias, A. S. (2010). Decorrelated neuronal firing in cortical microcircuits. *Science* 327, 584–587. doi:10.1126/science.1179867
- Effenberger, F. and Jost, J. (2015). Self-Organization in Balanced State Networks by STDP and Homeostatic Plasticity. *PLOS Computational Biology*
- Enel, P., Procyk, E., Quilodran, R., and Dominey, P. F. (2016). Reservoir Computing Properties of Neural Dynamics in Prefrontal Cortex. *PLOS Computational Biology* 12, e1004967. doi:10.1371/journal.pcbi.1004967
- Földiak, P. (1990). Forming sparse representations by local anti-Hebbian learning. *Biological Cybernetics*
- Franklin, J. L., Fickbohm, D. J., and Willard, A. L. (1992). Long-term regulation of neuronal calcium currents by prolonged changes of membrane potential. *Journal of Neuroscience* 12, 1726–1735. doi:10.1523/jneurosci.12-05-01726.1992
- Gallicchio, C. and Micheli, A. (2017). Echo state property of deep reservoir computing networks. *Cognitive Computation* 9, 337–350
- Gros, C. (2008). *Complex and Adaptive Dynamical Systems, a Primer* (Springer)
- Hinaut, X., Lance, F., Droin, C., Petit, M., Poiteau, G., and Dominey, P. F. (2015). Corticostriatal response selection in sentence production: Insights from neural network simulation with reservoir computing. *Brain and Language* 150, 54–68. doi:10.1016/j.bandl.2015.08.002
- Jaeger, H. (2002). *Short Term Memory in Echo State Networks*. Tech. rep., Fraunhofer Institute for Autonomous Intelligent Systems
- Lazar, A., Pipa, G., and Triesch, J. (2009). SORN: a self-organizing recurrent neural network. *Frontiers in Computational Neuroscience* 3
- Livi, L., Bianchi, F. M., and Alippi, C. (2018). Determination of the edge of criticality in echo state networks through Fisher information maximization. *IEEE Transactions on Neural Networks and Learning Systems* 29, 706–717
- Maass, W. and Markram, H. (2004). On the computational power of circuits of spiking neurons. *Journal of Computer and System Sciences* 69, 593–616. doi:10.1016/j.jcss.2004.04.001
- Maass, W., Natschläger, T., and Markram, H. (2002). Real-time computing without stable states: A new framework for neural computation based on perturbations. *Neural Computation* 14, 2531–2560. doi:10.1162/089976602760407955
- Marčenko, V. A. and Pastur, L. A. (1967). Distribution of Eigenvalues for some Sets of Random Matrices. *Mathematics of the USSR-Sbornik* 1, 457–483. doi:10.1070/sm1967v001n04abeh001994
- Massar, M. and Massar, S. (2013). Mean-field theory of echo state networks. *Physical Review E* 87, 42809. doi:10.1103/PhysRevE.87.042809
- Miner, D. and Triesch, J. (2016). Plasticity-Driven Self-Organization under Topological Constraints Accounts for Non-Random Features of Cortical Synaptic Wiring. *PLoS Computational Biology*

- Narayanan, R. and Johnston, D. (2012). Functional maps within a single neuron. *Journal of Neurophysiology* 108, 2343–2351. doi:10.1152/jn.00530.2012. PMID: 22933729
- Nikolić, D., Häusler, S., Singer, W., and Maass, W. (2009). Distributed fading memory for stimulus properties in the primary visual cortex. *PLoS biology* 7, e1000260
- Rajan, K. and Abbott, L. F. (2006). Eigenvalue Spectra of Random Matrices for Neural Networks. *Physical Review Letters* 97. doi:10.1103/physrevlett.97.188104
- Remme, M. W. and Wadman, W. J. (2012). Homeostatic scaling of excitability in recurrent neural networks. *PLoS Computational Biology* 8, 1002494. doi:10.1371/journal.pcbi.1002494
- [Dataset] Salinas, E. and Sejnowski, T. J. (2001). Correlated neuronal activity and the flow of neural information. doi:10.1038/35086012
- Schrauwen, B., Wardermann, M., Verstraeten, D., Steil, J. J., and Stroobandt, D. (2008). Improving reservoirs using intrinsic plasticity. *Neurocomputing* 71, 1159–1171. doi:10.1016/j.neucom.2007.12.020
- Schubert, F. and Gros, C. (2020). Local homeostatic regulation of the spectral radius of echo-state networks. *bioRxiv* doi:10.1101/2020.07.21.213660
- Sengupta, A. M. and Mitra, P. P. (1999). Distributions of singular values for some random matrices. *Physical Review E* 60, 3389
- Shen, J. (2001). On the singular values of Gaussian random matrices. *Linear Algebra and its Applications* 326, 1–14
- Spruston, N. (2008). Pyramidal neurons: dendritic structure and synaptic integration. *Nature Reviews Neuroscience* 9, 206–221. doi:10.1038/nrn2286
- Steil, J. J. (2007). Online reservoir adaptation by intrinsic plasticity for backpropagation-decorrelation and echo state learning. *Neural Networks* 20, 353–364. doi:10.1016/j.neunet.2007.04.011
- Stellwagen, D. and Malenka, R. C. (2006). Synaptic scaling mediated by glial TNF- $\alpha$ . *Nature* 440, 1054–1059. doi:10.1038/nature04671
- Sweeney, Y., Hellgren Kotaleski, J., and Hennig, M. H. (2015). A Diffusive Homeostatic Signal Maintains Neural Heterogeneity and Responsiveness in Cortical Networks. *PLOS Computational Biology* 11, e1004389. doi:10.1371/journal.pcbi.1004389
- Tao, T. and Vu, V. (2008). Random matrices: the circular law. *Communications in Contemporary Mathematics* 10, 261–307
- Tetzlaff, C. (2011). Synaptic scaling in combination with many generic plasticity mechanisms stabilizes circuit connectivity. *Frontiers in Computational Neuroscience* 5, 47. doi:10.3389/fncom.2011.00047
- Tetzlaff, T., Helias, M., Einevoll, G. T., and Diesmann, M. (2012). Decorrelation of Neural-Network Activity by Inhibitory Feedback. *PLoS Computational Biology* 8, 1002596. doi:10.1371/journal.pcbi.1002596
- Toyoizumi, T., Kaneko, M., Stryker, M. P., and Miller, K. D. (2014). Modeling the Dynamic Interaction of Hebbian and Homeostatic Plasticity. *Neuron* 84, 497–510. doi:10.1016/j.neuron.2014.09.036
- Trapp, P., Echeveste, R., and Gros, C. (2018). Ei balance emerges naturally from continuous hebbian learning in autonomous neural networks. *Scientific reports* 8, 1–12
- Triesch, J. (2007). Synergies between intrinsic and synaptic plasticity mechanisms. *Neural Computation* 19, 885–909. doi:10.1162/neco.2007.19.4.885
- [Dataset] Turrigiano, G. G. (2008). The Self-Tuning Neuron: Synaptic Scaling of Excitatory Synapses. doi:10.1016/j.cell.2008.10.008
- Turrigiano, G. G., Leslie, K. R., Desai, N. S., Rutherford, L. C., and Nelson, S. B. (1998). Activity-dependent scaling of quantal amplitude in neocortical neurons. *Nature* 391, 892–896. doi:10.1038/36103

- [Dataset] Turrigiano, G. G. and Nelson, S. B. (2000). Hebb and homeostasis in neuronal plasticity. doi:10.1016/S0959-4388(00)00091-X
- Usrey, W. M. and Reid, R. C. (1999). Synchronous Activity in the Visual System. *Annual Review of Physiology* 61, 435–456. doi:10.1146/annurev.physiol.61.1.435
- van Rossum, M. C. W., Bi, G. Q., and Turrigiano, G. G. (2000). Stable Hebbian Learning from Spike Timing-Dependent Plasticity. *Journal of Neuroscience* 20, 8812–8821
- Van Vreeswijk, C. and Sompolinsky, H. (1998). Chaotic Balanced State in a Model of Cortical Circuits. *Neural Computation* 10, 1321–1371. doi:10.1162/089976698300017214
- Wernecke, H., Sándor, B., and Gros, C. (2019). Chaos in time delay systems, an educational review. *arXiv preprint arXiv:1901.04826*
- Wick, S. D., Wiechert, M. T., Friedrich, R. W., and Riecke, H. (2010). Pattern orthogonalization via channel decorrelation by adaptive networks. *Journal of Computational Neuroscience* 28, 29–45. doi:10.1007/s10827-009-0183-1
- Zenke, F., Hennequin, G., and Gerstner, W. (2013). Synaptic Plasticity in Neural Networks Needs Homeostasis with a Fast Rate Detector. *PLoS Computational Biology* 9, 1003330. doi:10.1371/journal.pcbi.1003330

## 6 SUPPLEMENTARY FIGURES

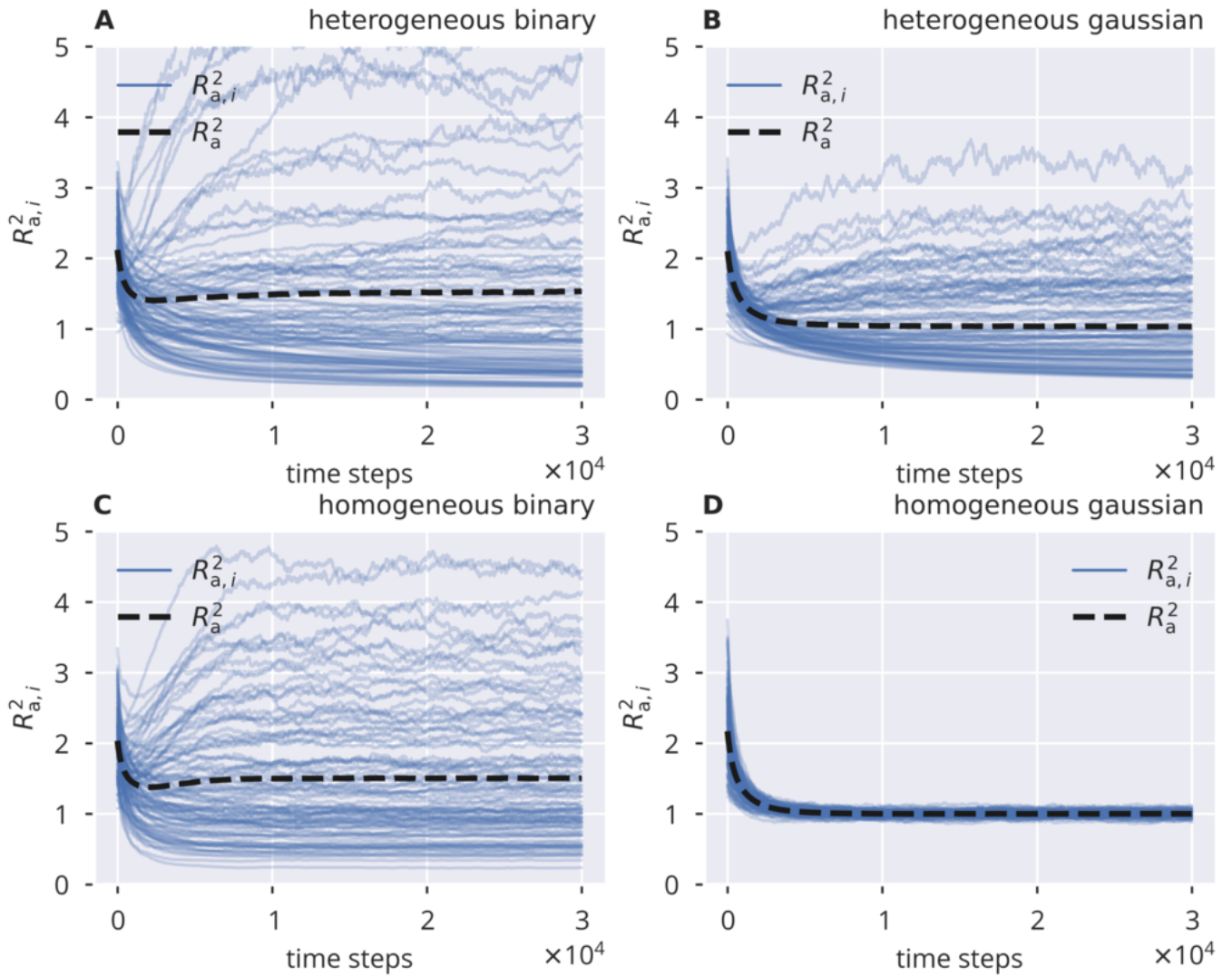


**Figure 11. Adaptation dynamics, flow control, local** Panels A–D show the dynamics of the square spectral radius  $R_a^2$  and local estimates  $R_{a,i}^2$  under local flow control for different input protocols, as given in the panel titles.

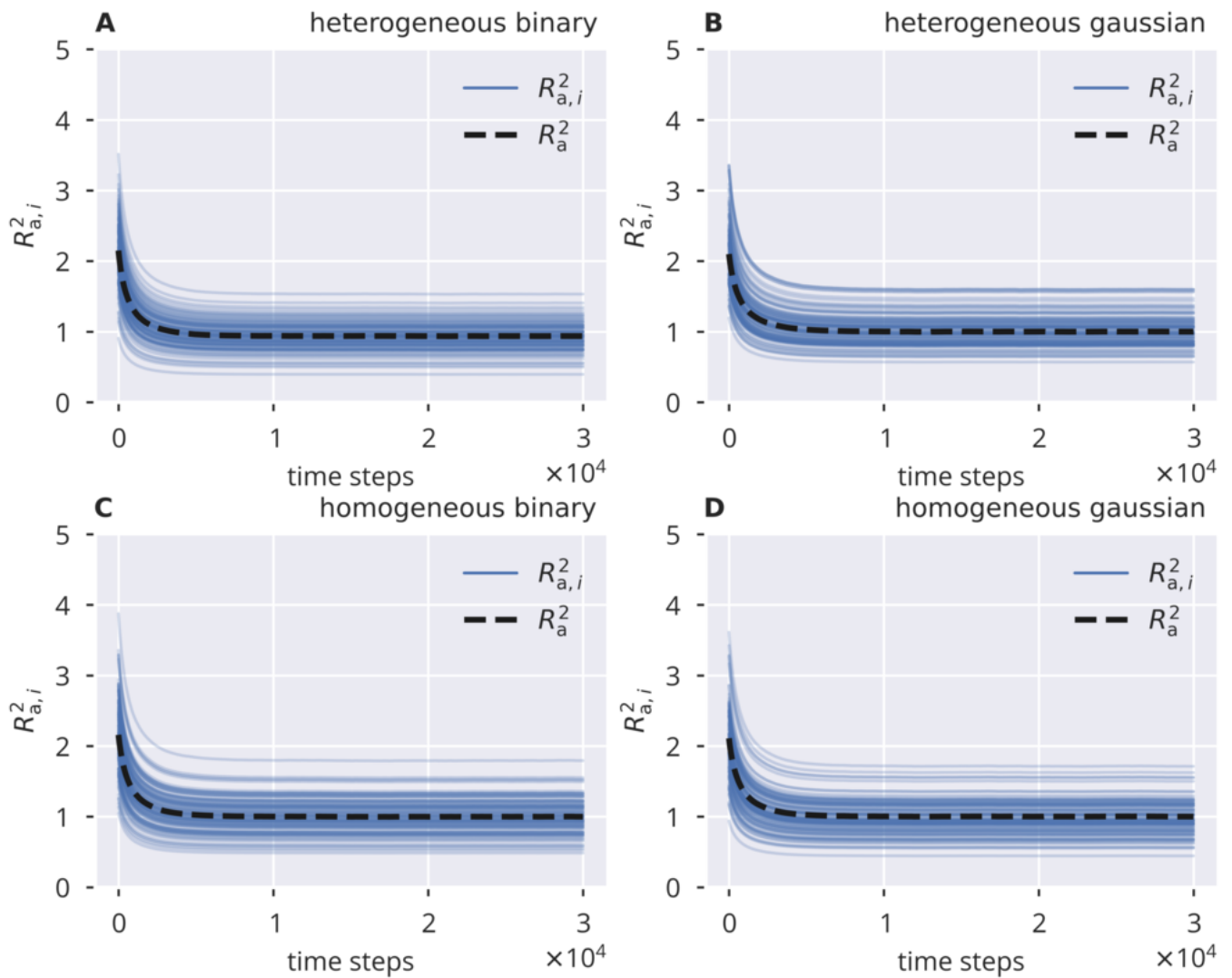


**Figure 12. Adaptation dynamics, flow control, global** Panels A–D show the dynamics of the square spectral radius  $R_a^2$  and local estimates  $R_{a,i}^2$  under global flow control for different input protocols, as given in the panel titles.

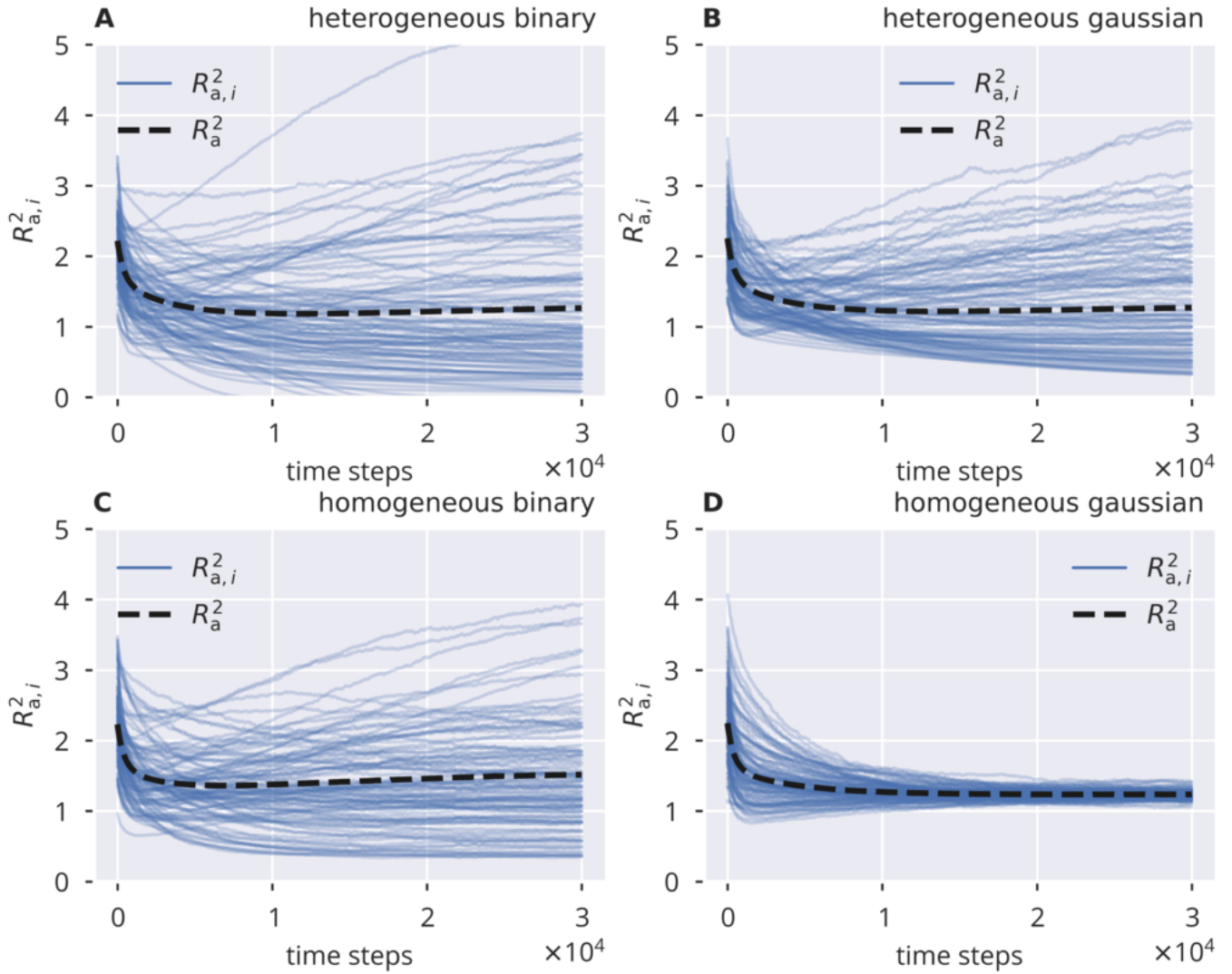


**Figure 13. Adaptation dynamics, variance control, local** Panels A–D show the dynamics of the square spectral radius  $R_a^2$  and local estimates  $R_{a,i}^2$ , under local variance control for different input protocols, as given in the panel titles.

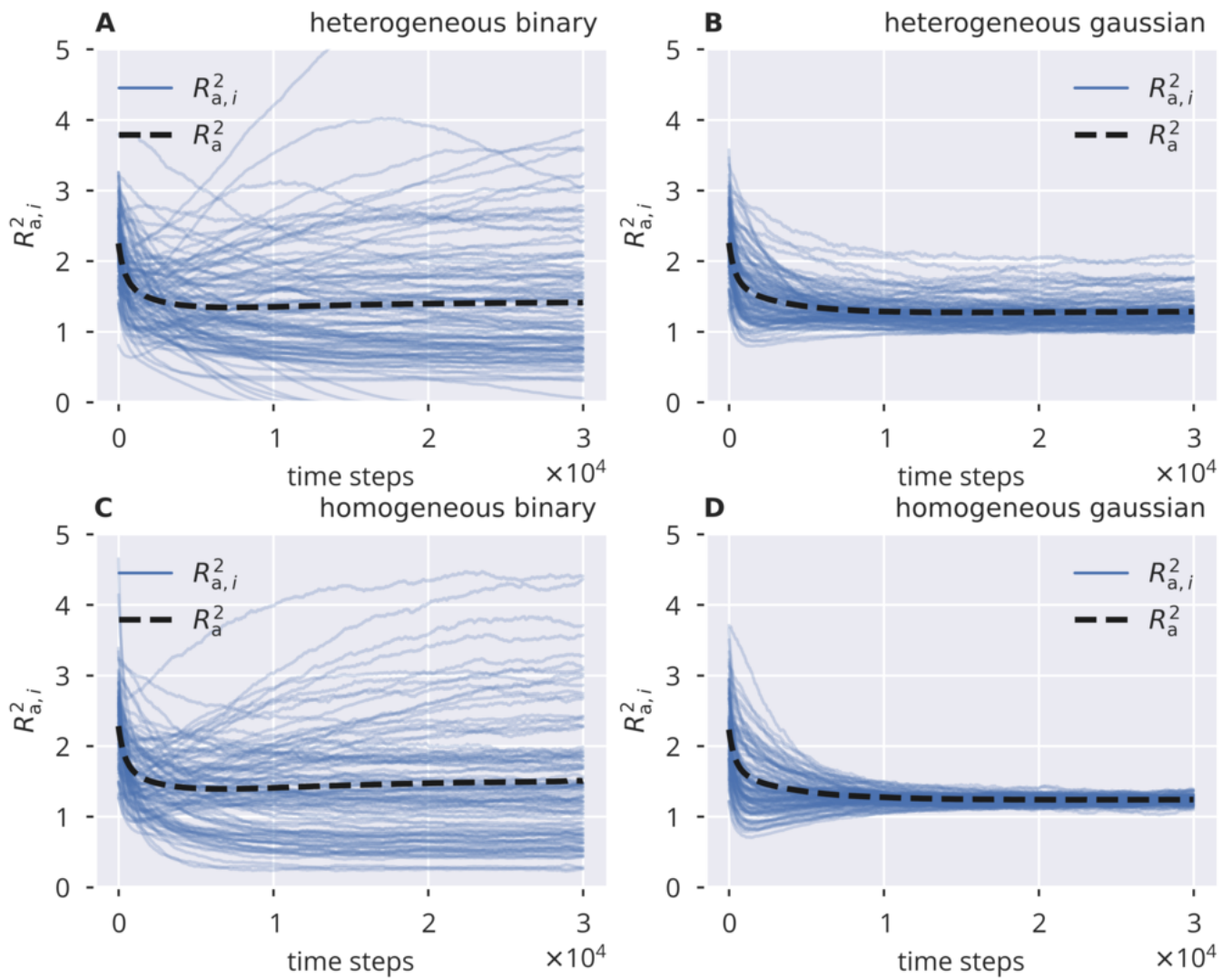


**Figure 14. Adaptation dynamics, variance control, global** Panels A–D show the dynamics of the square spectral radius  $R_a^2$  and local estimates  $R_{a,i}^2$  under global variance control for different input protocols, as given in the panel titles.

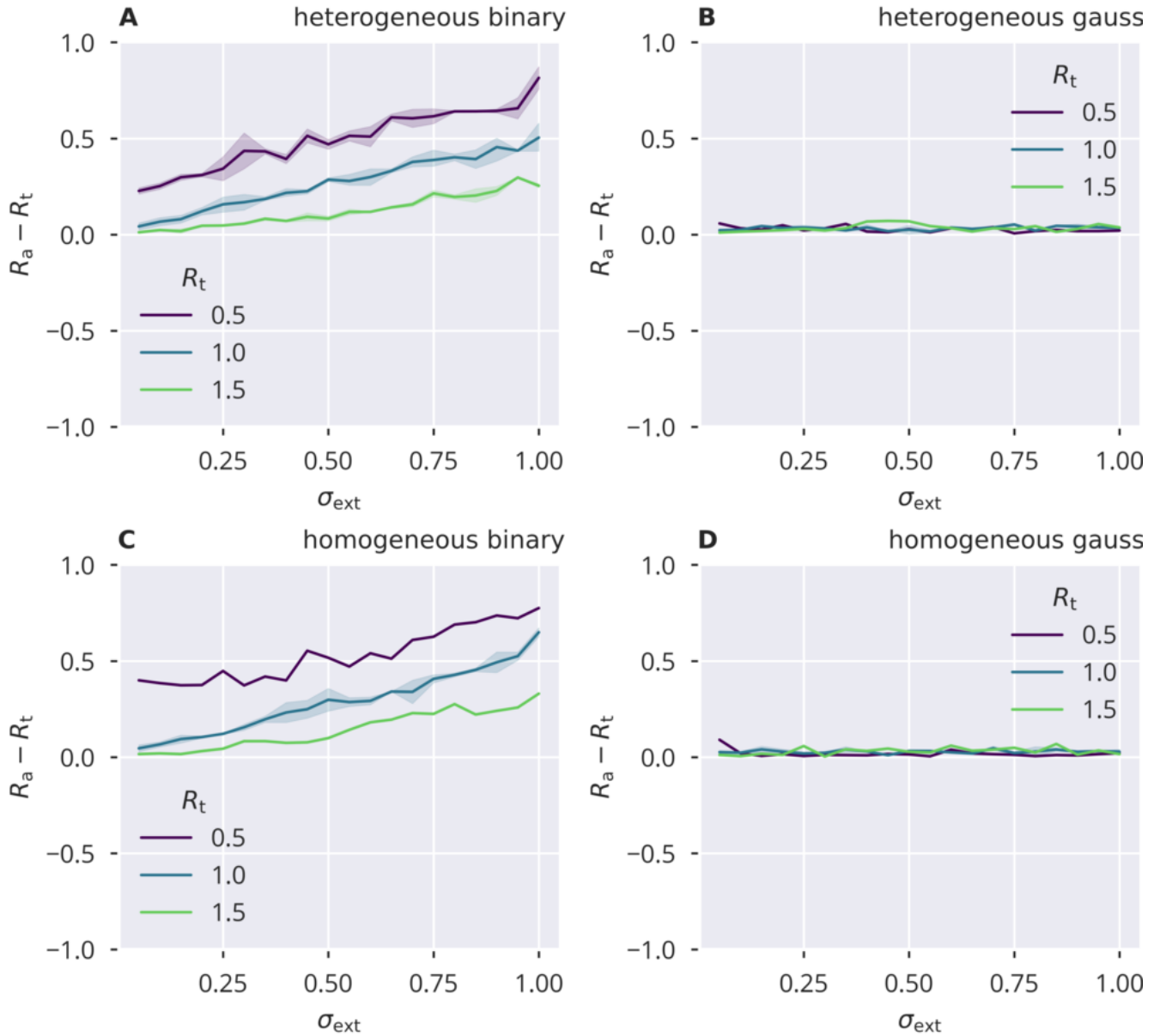


**Figure 15. Difference of the spectral radius after adaptation and the target spectral radius, flow control** For different standard deviations  $\sigma_{\text{ext}}$  of the external input, the error  $R_a - R_t$  between the resulting spectral radius  $R_a$  and the target spectral radius  $R_t$  was determined. Heterogeneous/homogeneous binary input (A/C) led to positive deviations from the target spectral radius for stronger external input. Heterogeneous/homogeneous Gaussian input (B/D) yielded perfect alignment between  $R_a$  and  $R_t$ . Local adaptation was used for both panels.



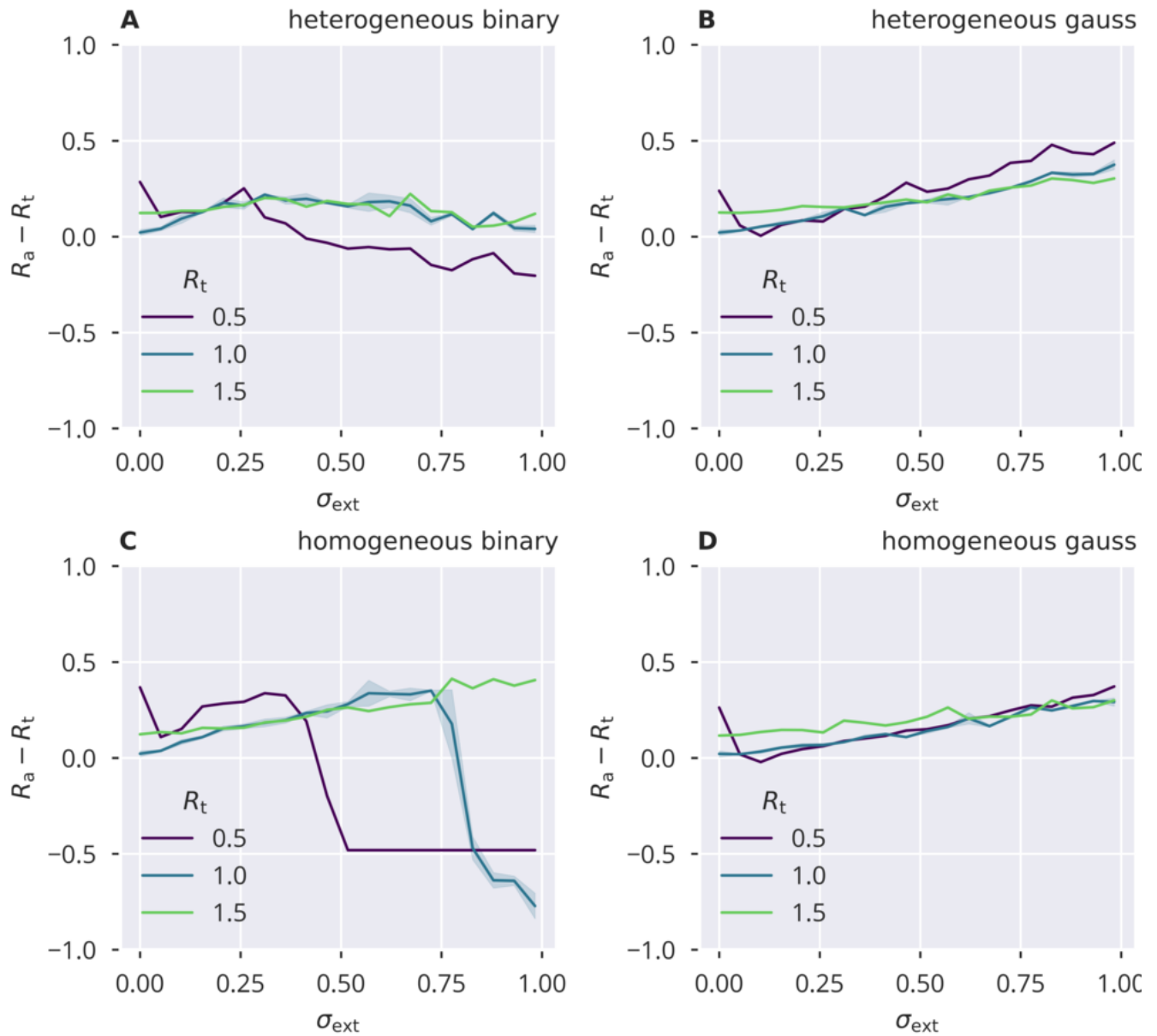


**Figure 16. Difference of the spectral radius after adaptation and the target spectral radius, variance control** For different standard deviations  $\sigma_{ext}$  of the external input, the error  $R_a - R_t$  between the resulting spectral radius  $R_a$  and the target spectral radius  $R_t$  was determined. Heterogeneous binary input (A) led to a good alignment. On the other hand, homogeneous binary input (C) caused strong deviation from the target for larger input. Heterogeneous/homogeneous Gaussian input (B/D) both resulted in positive deviations that increased for larger input strengths. Local adaptation was used for both panels.

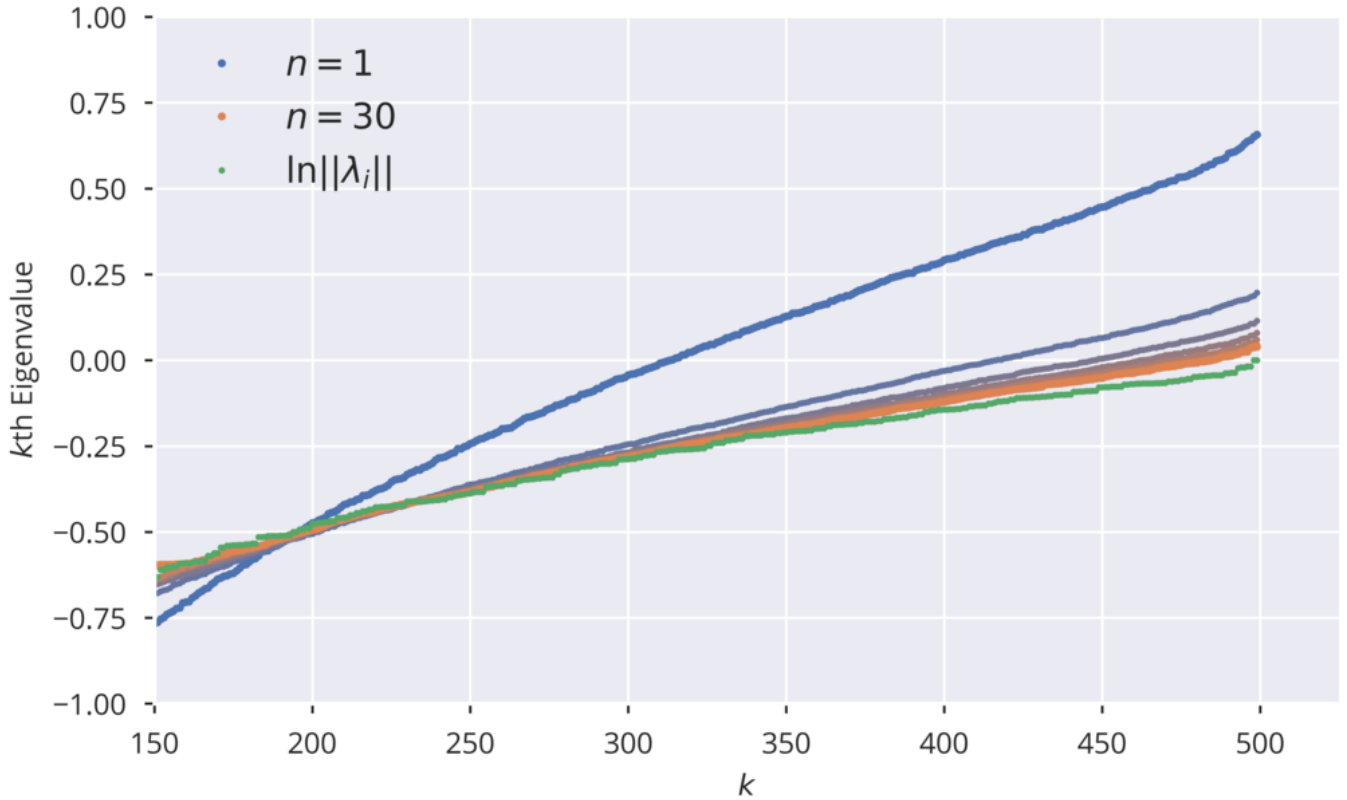


**Figure 17. Convergence of Lyapunov Spectrum.** Convergence of eigenvalues of  $\ln((\widehat{W}^n)^\dagger \widehat{W}^n)/(2n)$  for different  $n$ , as discussed in Section 2.6.  $\widehat{W}$  is a random Gaussian matrix which was rescaled to a spectral radius of one. Colors from blue to orange encode the exponent  $n$  ranging between 1 and 30. Green dots show the theoretical limit of  $\ln\|\lambda_i\|$ , where  $\lambda_i$  is the  $i$ th eigenvalue of  $\widehat{W}$ .

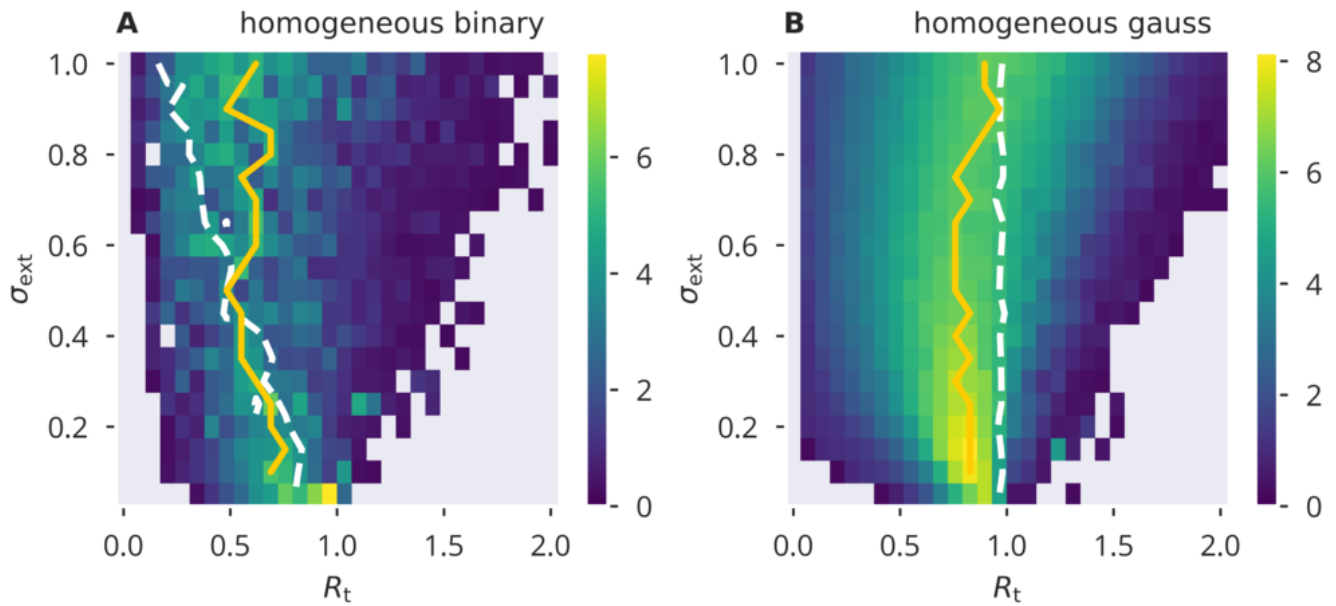


**Figure 18. XOR performance for flow control, homogeneous input.** Numerical results for the network performance under a time-delayed XOR task, as defined in Section 2.7, using homogeneous binary/Gaussian input. Shown are color-coded performance sweeps for the XOR-performance (18), averaged over five trials. The input has variance  $\sigma_{ext}^2$  and the target for the spectral radius  $R_t$ . A/B panels are for binary/Gaussian input protocols. Optimal performance for a given  $\sigma_{ext}$  is given by yellow solid lines, measured value of  $R_a = 1$  by white dashed lines.

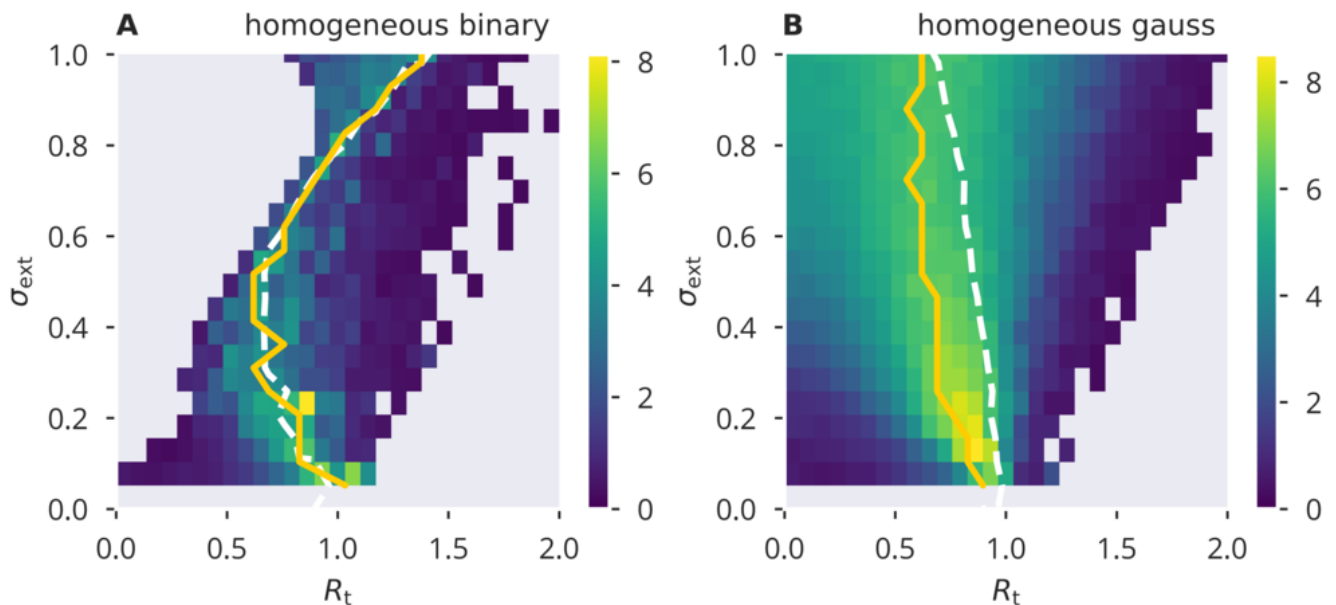


**Figure 19. XOR performance for variance control, homogeneous input.** Numerical results for the network performance under a time-delayed XOR task, as defined in Section 2.7, using homogeneous binary/Gaussian input. Shown are color-coded performance sweeps for the XOR-performance (18), averaged over five trials. The input has variance  $\sigma_{ext}^2$  and the target for the spectral radius  $R_t$ . A/B panels are for binary/Gaussian input protocols. Optimal performance for a given  $\sigma_{ext}$  is given by yellow solid lines, measured value of  $R_a = 1$  by white dashed lines.

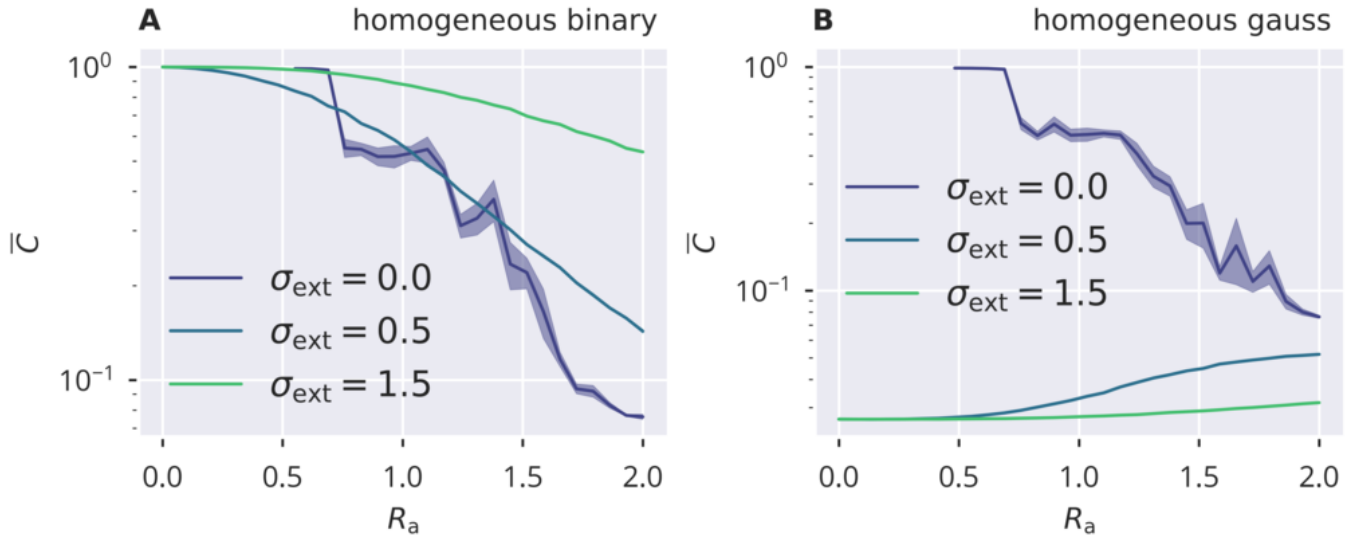


**Figure 20. Input induced activity correlations.** For homogeneous binary and Gaussian inputs (A/B), the dependency of mean activity cross correlations  $\bar{C}$ , see Eq. (21).  $\bar{C}$  is shown as a function of the target spectral radius  $R_a$ . Results are obtained for  $N = 500$  sites by averaging over five trials, with shadows indicating the accuracy. Correlations are due to finite-size effect for the autonomous case  $\sigma_{\text{ext}} = 0$ .

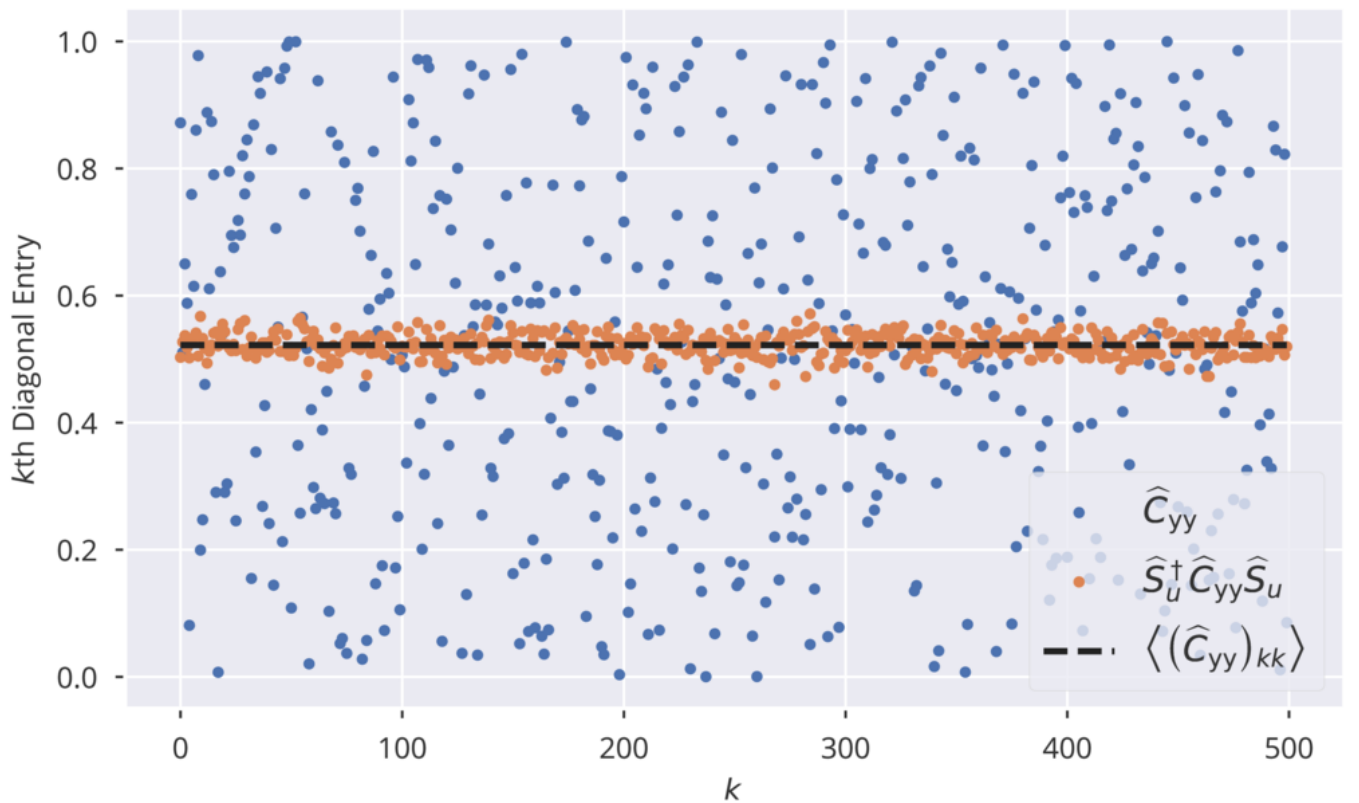


**Figure 21. Diagonal Elements of a randomly generated covariance matrix and its representation in the  $\hat{S}_u$  basis.**  $\hat{C}_{yy}$  is a diagonal matrix with diagonal entries randomly drawn from  $[0, 1]$ ,  $\hat{S}_u$  is the orthonormal eigenbasis of  $\hat{W}_a^\dagger \hat{W}_a$ , where  $\hat{W}_a$  is a random Gaussian matrix. The black dashed line denotes the average over the diagonal entries of  $\hat{C}_{yy}$ .